



1 **TITLE**

2 *The Italian contribution to the Synoptic Arctic Survey programme: the 2021 CASSANDRA cruise*
3 *(LB21) through the Greenland Sea Gyre along the 75°N transect*

4 **AUTHORS**

5 Manuel Bensi^{1*}, Giuseppe Civitarese¹, Diego Borme¹, Carmela Caroppo², Gabriella Caruso³,
6 Federica Cerino¹, Franco Decembrini³, Alessandra de Olazabal¹, Tommaso Diociauti¹, Michele
7 Giani¹, Vedrana Kovacevic¹, Martina Kralj¹, Angelina Lo Giudice³, Giovanna Maimone³, Marina
8 Monti¹, Maria Papale³, Luisa Patrolecco⁵, Elisa Putelli¹, Alessandro Ciro Rappazzo³, Federica
9 Relitti¹, Carmen Rizzo^{3,4}, Francesca Spataro⁵, Valentina Tirelli¹, Clara Turetta⁶, Maurizio Azzaro³

10

11 ¹ National Institute of Oceanography and Applied Geophysics, OGS, Trieste, Italy

12 ² Water Research Institute, National Research Council, CNR-IRSA, Taranto, Italy

13 ³ Institute of Polar Sciences, National Research Council, CNR-ISP, Messina, Italy

14 ⁴ Stazione Zoologica Anton Dohrn, Sicily Marine Centre, SZN-SMC, Messina, Italy

15 ⁵ Institute of Polar Sciences, National Research Council, CNR-ISP, Rome, Italy

16 ⁶ Institute of Polar Sciences, National Research Council, CNR-ISP, Venice, Italy

17 *Correspondence to: (mbensi@ogs.it)

18 **ABSTRACT**

19 In September 2021, as part of the Italian Arctic research programme, a multidisciplinary cruise
20 along the 75th parallel north through the Greenland Sea Gyre was conducted aboard the Italian
21 icebreaker Laura Bassi as part of the CASSANDRA project, which also contributed to the Synoptic
22 Arctic Survey (SAS) 2020/22. The cruise took place during the period of the lowest summer sea ice
23 extent ever measured. The data show strong horizontal gradients with temperatures between 1.5 °C
24 and 9.0 °C and salinity between 30 and 35. Warm and salty Atlantic Water (AW, $\theta > 3.0$ °C, S
25 around 35) dominates on the eastern side of the transect in the upper 500 m with surface
26 temperatures of 4.5–9.0 °C, while Polar Water (PW, $\theta < 0$ °C, S < 33) occupies the surface layer
27 (50–80 m) in the west. The intermediate layer (100–500 m) consists of mixed water, and below 500
28 m the deep water of the Greenland Sea and the Norwegian Sea predominates. The oxygen
29 enrichment is higher in the intermediate layers, while the values in deep layers and western regions
30 are lower ($< 300 \mu\text{mol kg}^{-1}$). A stratified upper layer (30–50 m deep) with low surface nutrients,
31 especially nitrate, is observed, while an accumulation of silicate occurs in deep water masses. The
32 surface water in the eastern part of the transect has high pH_T and total alkalinity values due to
33 photosynthesis and the presence of salty AW, while the fresh PW in the west has a lower alkalinity.
34 Respiratory activity and organic matter concentrations (particulate/dissolved organic carbon) vary
35 horizontally at the surface, decrease with depth, and increase slightly near the seafloor. A west-east
36 gradient is also observed for $\delta^{18}\text{O}$ and δD , with the ratios indicating the influence of freshwater at
37 the surface near the Greenland coast. The abundance of prokaryotes decreases from the photic zone



38 (< 100 m depth) to the sea floor. Carbohydrates and carboxylic acids are identified as well-utilised
39 polymers at every station and in every layer. Overall, the microbial enzyme patterns show a decrease
40 from the surface to deeper layers, with some hotspots of metabolic activity at 20-40 m and in the
41 aphotic layer. The enzyme patterns vary spatially, with activity peaks at the ends and in the middle
42 of the transect. Phytoplankton biomass, measured as chlorophyll-*a*, varies across the transect, with
43 higher values at its extremities. Micro-phytoplankton fraction dominates in PW, replacing the nano-
44 phytoplankton fraction, which is prevalent in AW, even at the interface between the two water
45 masses. Data of phytoplankton communities show low abundances and a dominance of nano-sized
46 organisms, with diatoms being more abundant in the western part. Microzooplankton represents an
47 important fraction of the planktonic community in this area, with tintinnids being the most important
48 groups along the transect. Micrometazoans and aloricate ciliates are more abundant in the AW,
49 resulting in higher biomass values at the eastern stations. Copepods are the most abundant
50 mesozooplanktonic taxon both at the surface and in the upper 100 m water layer (97% and 94% of
51 total mesozooplankton abundance, respectively), mainly represented by the genus *Calanus*.

52 The data are publicly available at the Italian Arctic Data Centre (IADC), see section Data
53 availability.

54 1 INTRODUCTION

55 The Greenland Sea, in the north Atlantic, is a region of deep ocean convection that contributes to
56 the Atlantic Meridional Overturning (AMOC) and the exchange of water masses between the
57 Atlantic and Arctic Oceans. Its sensitivity to climate change remains uncertain, as the ecosystems
58 of the subarctic Atlantic are particularly sensitive to global warming (Whitt, 2023). In fact, the
59 Greenland Sea serves also as a hub for heat, salts, nutrients, carbon, and organisms between the
60 Arctic, subarctic, and lower latitudes. Arctic and subarctic regions have experienced warming twice
61 as fast as global warming over the past 50 years (Rantanen et al., 2022). This has led to significant
62 environmental changes, including increasing wetness, reduced sea ice thickness and coverage,
63 changes in snow cover, thawing of permafrost, and melting of the Greenland ice sheet (Carmack et
64 al., 2015; Polyakov et al., 2017, 2023; Babb et al., 2023). These changes have created a positive
65 feedback loop known as "Arctic amplification" which is likely to intensify in the future. Despite its
66 crucial role in the global climate system, the Arctic Ocean remains poorly understood due to its
67 remote location, harsh weather, and seasonal ice cover. The Arctic Ocean receives heat through the
68 inflow of Atlantic Water (AW, with Temperature (T) > 0 °C). AW flows northward transported by
69 the Norwegian Atlantic Current (NAC) and the West Spitsbergen Current (WSC) along the eastern
70 slope of the North Atlantic and crosses the Greenland Sea and Fram Strait, where it is partly
71 deflected by the local circulation (Fig. 1). On the other hand, the Arctic outflow of Polar Water
72 (PW, T < 0 °C), together with the sea ice export from the Arctic, is driven by the East Greenland
73 Current (EGC, Chatterjee et al., 2018). Greenland freshwater flux shows a large seasonal variation,
74 with peaks in July (4-6 times higher than in winter), but also consistent increase since the 2000s
75 (Dukhovskoy et al., 2019). Changes in annual and multi-year sea ice trends are also an important
76 factor to consider when analysing the physical and biogeochemical conditions in the Greenland Sea.
77 Sea ice extent and thickness in the Arctic regions have continuously decreased over the last four
78 decades, and significant changes have also been observed in the Fram Strait since 2015 (de Steur et
79 al., 2023). Since 2020, however, sea ice extent in the Fram Strait and marginal seas has shown a
80 slight recovery in seasonal winter maxima (Onarheim et al., 2024). Open-ocean convection also



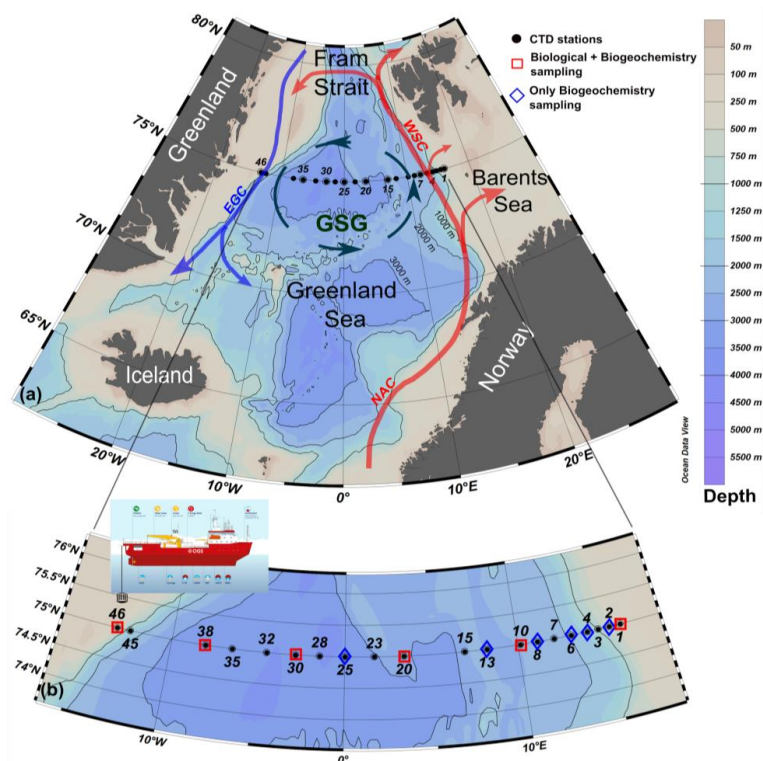
81 occurs in the Greenland Sea during winter seasons. It is thought to represent a significant proportion
82 of dense water production for the regions, even though a large variability in this process has been
83 observed in recent decades, including changes in the depth of convection (Simpkins, 2019; Brakstad
84 et al., 2019). Overall, the predominant atmospheric conditions over the Arctic are characterised by
85 the presence of high pressure (i.e., Polar High) over the western Arctic and low pressure over the
86 Siberian region, which trigger the main anticyclonic wind regime. However, after 2007 a secondary
87 dipole, characterised by higher sea level pressure over the Beaufort Gyre and the Canadian
88 Archipelago along with lower sea level pressure over the Siberian Arctic, became dominantly
89 positive, favouring reduced flows into the Arctic through the Fram Strait along with enhanced
90 inflows through the Barents Sea Opening (Polyakov et al., 2023). Consequently, from 2007 to 2021,
91 the predominant cyclonic atmospheric regime over the Arctic Ocean pushed large amounts of
92 freshwater from the Siberian shelves into the Beaufort Gyre (Polyakov et al., 2023).

93 The cyclonic Greenland Sea Gyre (GSG) in the central Greenland Sea, which is mainly driven by
94 large-scale cyclonic winds, contributes to the regulation of the inflow and outflow of AW and PW
95 between the Atlantic and Arctic Oceans (Chatterjee et al., 2018). The GSG, and the North Atlantic
96 subpolar gyre (SPG), south of Iceland, have large implications for the large-scale changes in the
97 subpolar and polar marine environment. A strong GSG triggers a northwestward shift of the
98 subpolar front, which intensifies the poleward transport of Atlantic water towards the Fram Strait,
99 Barents Sea and Arctic Ocean (Chatterjee et al., 2018). In contrast, a weak phase (i.e., a negative
100 index, see Fan et al., 2023) in the SPG enables the northward expansion of subtropical warm and
101 saline waters, while a strong SPG feeds cold and fresh subpolar waters into the Atlantic inflow.

102



103



104

105 **Figure 1** - (a) Schematic of the general circulation in the Greenland Sea (GSG-Greenland Sea Gyre; WSC-West
106 Spitsbergen Current; EGC-East Greenland Current; NAC- Norwegian Atlantic Current). (b) Distribution of
107 hydrological (CTD) stations conducted during the LB21 CASSANDRA cruise (29 August -14 September 2021) with
108 the positions of the physical (black dots), biogeochemical and biological stations (blue and red symbols).

109 A time lag of 3-5 years is expected for the thermohaline anomalies to propagate in the Nordic seas
110 (Fan et al., 2023) from the sub polar regions. In other words: while the GSG regulates the AW
111 inflow into the Arctic, the SPG modulates the proportion of subtropical and subpolar waters moving
112 at high latitudes. Wind forcing and heat loss combine to drive the full variability of the flow and
113 water mass transformations in the region (Smedsrud et al., 2022).

114 The anomalous inflow of AW from the Nordic seas and the subpolar regions is referred to a process
115 called Atlantification, which has various direct and indirect effects on the Arctic environment. This
116 process has intensified since the 2000s, leading to, among other effects, increasing anomalies in
117 temperature and salinity in the upper layer, a reduction in sea ice cover, reduced stratification of the
118 upper ocean, increased primary production and a shift of the summer bloom to earlier periods,
119 changes in the phenology, distribution and community composition of zooplankton, and spreading
120 of subarctic species (Polyakov et al., 2017; Ingvaldsen et al., 2021; Csapò et al., 2021). Microbial
121 communities are also affected by the co-occurrence of Atlantification and Arctic amplification, as
122 pointed out by recent observations (Ahme et al., 2023; Priest et al., 2023). Microorganisms are
123 pivotal drivers in all the earth ecosystems, as primary degraders of organic matter and main players
124 in nutrient cycling. They are thus particularly sensitive to the external environmental conditions and



125 as such, play a role of optimal sentinels of global changes and trends (Caruso et al., 2016). Distinct
126 bacterial communities have been reported between Atlantic- and Arctic-derived waters (Carter-
127 Gates et al., 2020), and a direct effect of organic matter dissolution from the sea ice on the microbial
128 diversity has been demonstrated, by documenting the occurrence of diverse bacterial assemblages
129 between sea-ice and seawater (Yergeau et al., 2017). The Greenland Sea, like other Nordic Seas, is
130 a sink for atmospheric CO₂ during the year (Skjelvan et al., 2005). The annual flux of CO₂ absorbed
131 by the sea has been estimated at 53 gC m⁻² yr⁻¹. Of this amount, about half was attributed to the flux
132 caused by heat loss and the other half to biological production (Anderson et al., 2000). Higher
133 estimates of annual fluxes, ranging from 40 to 85 gC m⁻² yr⁻¹, were presented by Skjelvan et al.
134 (2005 and reference therein). Total carbon in surface waters varies seasonally because of physical
135 and biological processes that influence the amount of carbon exported to deep waters (von
136 Bodungen et al., 1995; Noji et al., 1999). The mixing of the open ocean contributes to the transport
137 of carbon from the surface to the deep interior. As a result of the increasing CO₂ input from the
138 atmosphere, the pH in the Nordic Seas has decreased by ~0.0028 units per year in the period 1981-
139 2019 (Frasner et al., 2022).

140 Here, we present data and main results obtained in the framework of the CASSANDRA (*advanCing*
141 *knowledge on the present Arctic Ocean by chemical-phySical, biogeochemical and biological*
142 *obServAtioNs to preDict the futuRe ChAnGes*) project funded by the Italian Arctic Research
143 Programme (<https://www.programmaricercaartico.it/>). CASSANDRA contributed to the Synoptic
144 Arctic Survey (SAS) by investigating the historical zonal transect at 75°N through the Greenland
145 Sea Gyre during the summer of 2021 (29 August - 14 September). The SAS initiative aims to
146 quantify the current state of the Arctic Ocean and its changes, focusing on water masses,
147 ecosystems, and the carbon cycle (see <https://synopticarcticsurvey.w.uib.no/>). SAS sees the
148 participation of 11 countries in 25 Arctic cruises.

149 2 DATA and METHODS

150 The LB21 CASSANDRA cruise (hereinafter, LB21 cruise) was carried out between 29 August 2021
151 (Longyearbyen, Svalbard) and 14 September 2021 (Bergen, Norway) on board the icebreaker Laura
152 Bassi (<https://www.ogs.it/en/research-vessel-laura-bassi>). All methods used for the CASSANDRA
153 activities were in line with the recommendations of the SAS and Go-Ship programme
154 (<https://www.go-ship.org/>), the latter including the 75°N transect. This approach was chosen to
155 obtain data that were as comparable as possible to other the SAS programme cruises. During the
156 LB21 cruise, a total of 28 vertical Conductivity-Temperature-Depth (CTD) profiles were conducted
157 at 20 hydrological stations (some stations include repeated casts). Of these, biogeochemical and
158 biological data were also collected at 12 and 6 stations, respectively (see Fig. 1). Unfortunately,
159 some technical problems and 2 days of adverse meteorological conditions in the middle of the cruise
160 prevented the completion of all planned stations. Some of the figures presented here were created
161 with Ocean Data View (Schlitzer, 2024).

162 2.1 Hydrographic data

163 All hydrographic profiles were recorded with a Seabird SBE911 plus, equipped with some additional
164 sensors. CTD measurements provide vertical profiles of temperature (T) and conductivity (C)
165 approaching the seafloor to ~ 5–10 m, depending on sea conditions. Potential temperature (θ),



166 salinity (S), and potential density anomaly (σ_θ , referred to 0 dbar) were calculated from *in situ* data
167 using the MATLAB toolbox TEOS-10 (Gibbs SeaWater Oceanographic Toolbox) including the
168 thermodynamic equations for seawater (<http://www.teos-10.org/software.htm>). Dissolved Oxygen
169 concentration was measured using an SBE43 sensor. T and S data were quality checked and
170 averaged every 1 dbar, with overall accuracy within ± 0.002 °C for T, ± 0.005 for S and 2% of
171 saturation for oxygen. Fluorescence and turbidity in the water column were measured with optical
172 sensors WET Labs ECO-AFL/FL. Water sampling was carried out using a rosette system equipped
173 with 24 10-liter Niskin bottles.

174 2.2 Biogeochemistry data

175 The chemistry of seawater was investigated at 12 stations from discrete water samples (Fig. 1) by
176 measuring dissolved oxygen, nutrients (nitrite, nitrate, phosphate, silicate), dissolved and particulate
177 Carbon (DOC and POC), total dissolved nitrogen and phosphorus (TDN and TDP); $\delta^{18}\text{O}$ and δD of
178 H_2O ; inorganic carbonate system characterization by total alkalinity, pH_T and derived parameters.
179 The dissolved oxygen concentration (DO) was determined by a potentiometric Winkler titration
180 (Oudot et al., 1988; Grasshoff et al., 1999). Samples for inorganic nutrients (nitrite - NO_2 , nitrate -
181 NO_3 , ammonium - NH_4 , phosphate - PO_4 and silicate - $\text{Si}(\text{OH})_4$) were collected and analysed as
182 described in Ingrosso et al. (2016a) using a four-channel Continuous Flow Analyzer QuAAtro (Seal
183 Analytical Inc., Mequon, WI, USA) autoanalyzer. Detection limits were $0.01 \mu\text{mol L}^{-1}$, $0.02 \mu\text{mol}$
184 L^{-1} , $0.03 \mu\text{mol L}^{-1}$, $0.01 \mu\text{mol L}^{-1}$ and $0.01 \mu\text{mol L}^{-1}$ for NO_2 , NO_3 , NH_4 , PO_4 and $\text{Si}(\text{OH})_4$,
185 respectively. DON and DOP were calculated as the difference between dissolved total phosphorus
186 (TDP) and PO_4 and between dissolved total nitrogen (TDN) and dissolved inorganic nitrogen (DIN
187 = $\text{NO}_3 + \text{NO}_2 + \text{NH}_4$), respectively. TDP and TDN were determined as PO_4 and NO_3 , respectively,
188 after quantitative conversion to inorganic P and N by persulfate oxidation (Hansen and Koroleff,
189 1999). The accuracy and precision of the analytical procedures are annually checked through the
190 quality assurance program (AQ1) QUASIMEME Laboratory Performance Studies (Wageningen,
191 The Netherlands) and internal quality control samples were used during each analysis. Samples for
192 pH_T analysis were collected and analysed on board as described in Ingrosso et al. (2016b) and Urbini
193 et al. (2020) using a spectrophotometer (Varian Cary 50 UV-visible). The results were expressed
194 on the 'pH total hydrogen ion scale' (pH_T) at 25°C, with a reproducibility of 0.0048, determined by
195 replicates from the same Niskin bottles. To measure total alkalinity (A_T , $\mu\text{mol kgSW}^{-1}$), water
196 samples were collected and analysed as described in Ingrosso et al. (2016a) and Urbini et al. (2020)
197 using the seawater certified reference materials (CRMs) for TCO_2 and A_T supplied by Prof. A.G.
198 Dickson, Scripps Institute of Oceanography, USA (Batch number #185) to calibrate HCl for
199 analyses. A_T precision and the accuracy were less than $\pm 2.0 \mu\text{mol kg}^{-1}$, assessed by analysing
200 CRMs. All other carbonate system parameters, including pH_T at *in situ* temperature, seawater partial
201 pressure of CO_2 (pCO_2), TCO_2 , and aragonite saturation state (Ω_ar) were calculated using the
202 CO_2Sys program as described in Urbini et al. (2020). The estimated uncertainties were: ± 0.005 for
203 pH_T at *in situ* temperature, $\pm 7.8 \mu\text{atm}$ for pCO_2 , $\pm 5.6 \mu\text{mol kg}^{-1}$ for TCO_2 and ± 0.12 for aragonite
204 saturation state. Samples for stable isotopic composition of dissolved inorganic carbon ($\delta^{13}\text{C-DIC}$)
205 were collected in 12-mL Exetainer® (Labco Limited, Ceredigion, UK) evacuated glass tubes,
206 containing 2 μL of saturated HgCl_2 . Samples were stored at 4 °C in the dark until analysis was
207 performed as described in Relitti et al. (2020). To determine the optimal extraction procedure for



208 water samples, two standard Na_2CO_3 solutions were prepared with a known ^{13}C value of $-10.8 \pm$
209 0.1 ‰ ($k=1$) and $-4.2 \pm 0.1 \text{ ‰}$ ($k=1$), respectively. The stable isotopic composition of dissolved
210 inorganic carbon is given conventionally in δ -notation in per mil deviation (‰) from the Vienna
211 Peed Dee belemnite (VPDB) standard.

212 For POC concentrations filters were freeze-dried and subsampled by punching 18% of the 45 mm
213 filter area and fitted into silver capsules/boats. The subsamples were treated with 1M HCl to remove
214 inorganic carbon and then placed into an oven at 60 C until dry. Afterwards, the samples were
215 wrapped in tin capsules/boats to aid combustion during analysis. The samples were analyzed with
216 a Thermo Fisher elemental analyzer (FLASH 2000 CHNS = O) coupled with a Thermo Finnigan
217 DeltaC isotope ratio mass spectrometer (IRMS).

218 Water samples for DOC analyses were filtered aboard, immediately after collection, through
219 precombusted (4 h at 480 °C) Whatman GF/F glass fibre filters (0.7 μm nominal pore size).
220 Filtration was performed by using a disposable polycarbonate syringe and a polypropylene 25 mm
221 filter holder (Nuclepore), to prevent atmospheric contamination. Filtered samples were stored in 25
222 mL high density polyethylene (HDPE) bottles (previously treated with HNO_3 1.2 M at 50 °C for 1
223 h) which were quickly frozen in an aluminium block at -20 °C. In the laboratory, filtered samples
224 were thawed, acidified to $\text{pH} = 2$ with ultrapure HCl and purged with N_2 for about 10 min to remove
225 inorganic carbon, as outlined in Pettine et al. (2001). Dissolved organic carbon (DOC) was assayed
226 by high temperature catalytic oxidation (HTCO) using a Shimadzu TOC-L series analyser.

227 Samples for stable isotope ratio measurements in seawater were collected in 5 mL amber glass
228 bottles. The bottles were filled to avoid the presence of air, immediately sealed and stored at a
229 temperature of 4 °C until the analyses. Analyses were performed by means of a Thermo DeltaV-
230 Advantage mass spectrometer equipped with a gas-bench. For the analysis, a quantity of 200 μL of
231 water sample was used in a glass vial firmly closed with a membrane cap. The samples were flushed
232 with a gas mixture of 2% H_2 in helium with a purity of 99.998 and analysed to determine δD .
233 Immediately after the δD analyses, the same samples were flushed with a gas mixture of 0.4% CO_2
234 in helium with a purity of 99.998 and analysed to determine $\delta^{18}\text{O}$ after 20 hours of equilibration.
235 All samples were measured at least in triplicate and the isotopic data are the mean of consistent
236 results. The standard deviation of our results is always 0.50 ‰ and 0.06 ‰ or better for δD and $\delta^{18}\text{O}$,
237 respectively. The SMOW2 and SLAP2 isotopic standards were used as a reference together with a
238 ‘home-made’ standard. The home-made standard is analysed every 3 measurements (3 replicates of
239 a single sample) to assess the stability of the measurements. The isotopic composition is expressed
240 as:

$$241 \quad \delta X = [(R_s - R_r) / R_r] \times 1000$$

242 where δX represents δD or $\delta^{18}\text{O}$, $R = \text{D}/\text{H}$ or $^{18}\text{O}/^{16}\text{O}$ in the sample (s) and in the reference (r),
243 respectively.



244 **2.3 Phytoplankton data**

245 **2.3.1 Total and size-fractionated chlorophyll a (chl-a)**

246 Chlorophyll *a* (chl-*a*) and phaeopigment (phaeo) concentration were measured fluorometrically.
247 Samples were filtered on Whatman GF/F glass-fiber and polycarbonate membranes to separate three
248 size fractions: micro-phytoplankton (> 10 µm), nano-phytoplankton (10–2.0 µm) and pico-
249 phytoplankton (2.0–0.45 µm) as reported in Decembrini et al. (2021).

250 **2.3.2 Utermöhl phytoplankton**

251 For the determination of Utermöhl phytoplankton (i.e., all species/taxa detectable by light
252 microscopy, thus excluding prokaryotic phytoplankton and the majority of picoeukaryotes < 1 µm),
253 500-mL water samples were collected in opaque polyethylene bottles and immediately fixed with
254 pre-filtered and neutralised formaldehyde (1.6% final concentration) (Thronsen, 1978). Inverted
255 microscopes equipped with phase contrast (Zeiss Axiovert 200M and Leica DMi8) were used for
256 the taxonomic identification analysing a variable volume of sample (10-50 mL), according to the
257 Utermöhl method (Zingone et al., 2010). Counting was performed along transects across the
258 microscope chambers at a magnification of 400x for small (5-20 µm) or very abundant species and
259 observing half of the sedimentation chamber at a magnification of 200x for less abundant
260 microphytoplankton (> 20 µm). The abundance was expressed as the number of cells per liter (cells
261 L⁻¹). The minimum value of the counted cells was 200 cells per sample for a confidence limit of
262 14% (Andersen & Thronsen, 2004).

263 **2.4 Zooplankton data**

264 **2.4.1 Microzooplankton**

265 Microzooplankton (MZP) samples were collected in six stations at different depths depending on
266 water column vertical profiles (Fig. 1). For MZP analyses, 10 L of seawater were reverse filtered
267 through a 10 µm mesh to reduce the volume to 250 mL and immediately fixed with buffered
268 formaldehyde (1.6% final concentration). Subsamples (50 mL) were then examined in a settling
269 chamber using an inverted microscope (magnification 200x) (Leitz Labovert, Leica DMI 300B),
270 following the Utermöhl method (1958). The entire surface of the chamber was examined. Among
271 the MZP community, five main groups were considered: heterotrophic dinoflagellates, aloricate
272 ciliates, tintinnids, micrometazoans and other rare protozoans. Tintinnids empty loricae were not
273 differentiated from filled loricae because the tintinnid protoplasts are attached to the lorica by fragile
274 strands that can easily detach during the collection and fixing of the samples. For each taxon, the
275 biomass was estimated by measuring the linear dimensions of each organism with an eyepiece scale
276 and relating the shapes to standard geometric figures. Cell volumes were converted into carbon
277 values using the appropriate conversion factors, as follows: aloricate ciliates, pg C cell⁻¹ as µm³ x
278 0.14 (Putt and Stoecker, 1989); tintinnids, pg C cell⁻¹ as µm³ x 0.053 + 444.5 (Verity and Langdon,
279 1984); athecate heterotrophic dinoflagellates, pg C cell⁻¹ as µm³ x 0.11 (Edler, 1979); thecate
280 heterotrophic dinoflagellates, pg C cell⁻¹ as µm³ x 0.13 (Edler, 1979); other protozoans, pg C cell⁻¹
281 as µm³ x 0.08 (Beers and Stewart, 1970).



282 **2.4.2 Mesozooplankton**

283 Three hauls were conducted at six stations (Fig. 1): one horizontally at the surface with the Manta
284 net (333 μm , 0.098 m^2 net opening) and 2 vertically (from 100 m depth to the surface) with the
285 WP2 net. A Hydrobios flowmeter mounted in the net opening was used to measure the volume of
286 seawater filtered through each net. Immediately after the catch, samples were treated to estimate
287 biomass, taxa composition and abundance of the zooplanktonic community. Samples collected with
288 the Manta net were split by using the Huntsman beaker technique (van Guelpen et al., 1982) and
289 treated as follows: half of the sample was fractionated by passing it through a series of steel sieves
290 with decreasing mesh size (> 2 mm; 2-1 mm; 1-0.5 mm; 0.5-0.2 mm) and immediately frozen at -
291 20°C for biomass analysis, $\frac{1}{4}$ was fixed and preserved in a seawater-buffered formaldehyde solution
292 (4% final concentration) for later determination of taxa composition and abundance and $\frac{1}{4}$ was fixed
293 in 96% ethanol for molecular analysis (data not shown in this manuscript). Samples collected with
294 the WP2 net were treated as follows: one sample was entirely fractionated and frozen at -20°C for
295 biomass analysis using the same procedure as the Manta net samples, and one sample was split in
296 half and fixed in seawater-buffered formaldehyde solution (4% final concentration) and 96%
297 ethanol, respectively. In the laboratory, to estimate biomass (dry mass), each size fraction was
298 resuspended in a small volume of filtered seawater and dewatered by vacuum filtration on pre-dried
299 and weighed GF/C filters (47 mm diameter) after being briefly rinsed with distilled water to remove
300 the salts of the seawater (Postel et al., 2000). Each filter was then placed in a small plastic Petri dish
301 and dried in an oven at 60 °C for 24 hours or longer until completely dry and weighed on an
302 electronic microbalance. The fixed samples were concentrated to remove the formaldehyde, and the
303 organisms were suspended in filtered seawater and carefully passed through the same set of sieves
304 used for the biomass. Depending on the abundance, the organisms present in the subsamples or in
305 the entire fractionated sample were counted and identified (Copepoda, Chetognata, Mollusca, and
306 others) under stereo-microscopes (Leica 165C :120x; Leica 205C: 160x).

307 **2.5 Microbiological data**

308 **2.5.1 Prokaryotic biomass, viable and dead cells, respiring cells**

309 The microbial components were investigated by using different approaches. The detailed
310 methodological procedures for assessing prokaryotic cell abundances, biomass and morphometric
311 features are reported by La Ferla et al. (2012). The viability of prokaryotic cells quantified by the
312 Live/Dead Bac Light Bacterial Viability Kit™ and the number of respiring cells quantified by the
313 Bac Light Redox Sensor CTC Vitality Kit™ were estimated as reported by Azzaro et al. (2022).

314 **2.5.2 Physiological profiles of microbial community**

315 Physiological profiles were determined by the Biolog EcoPlate™ microplate assay. The metabolic
316 potentials of bacterial assemblages were quantified as the optical density (OD) values of the
317 formazan produced by oxidation of the 31 carbon sources included in the Biolog Ecoplates. The
318 absorbance was recorded at 590 nm excitation wavelengths using a compact plate reader Byonoy
319 Absorbance 9 and spectrophotometrically measured according to Azzaro et al. (2022) and
320 references therein.



321 **2.5.3 Microbial activities involved in organic matter decomposition and mineralization**
322 **(enzymatic and respiratory activity rates)**

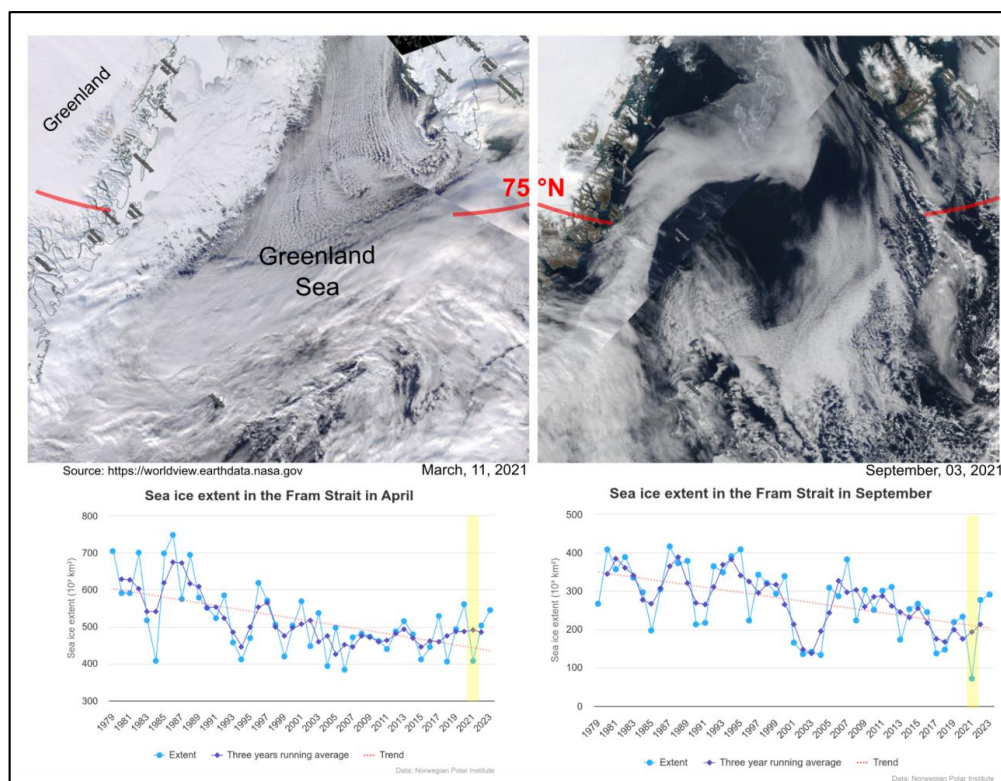
323 The potential decomposition rates of organic polymers (proteins, polysaccharides and organic
324 phosphates), mediated by the microbial enzymes leucine aminopeptidase (LAP), beta glucosidase
325 (GLU) and alkaline phosphatase (AP) respectively, were estimated by incubation with fluorogenic
326 substrates derived from methylcoumarin (MCA) and methylumbelliferone (MUF), as reported by
327 Hoppe (1993), adapted by Caruso et al. (2020). Fluorescence readings were converted into
328 enzymatic activity rates and expressed as the maximum rate (V_{max}) of hydrolysis of the substrates,
329 in $nM h^{-1}$.

330 **2.5.4 Respiratory activity**

331 The respiration rates were measured by the Electron Transport System activity (ETS) assay. This
332 method is based on the conversion of tetrazolium salt into formazan. The detailed methodological
333 procedures were reported by Azzaro et al. (2006, 2021) and references therein.

334 **3 RESULTS**

335 The LB21 cruise (see Fig. 1) was conducted in early September, when the seasonal minimum of sea
336 ice extent is recorded in the Arctic and sub-Arctic regions (Fig. 2). The ice extent in the Fram Strait
337 fluctuates from year to year. In the long term, the lowest extent in September was recorded exactly
338 in 2021, the highest in 1987. After 2021, a recovery of the summer seasonal sea ice extent was
339 observed. For winter, the lowest extent was observed in 2006, the highest in 1986. Our cruise
340 therefore took place during the period of the lowest summer sea ice extent measured to date.



341

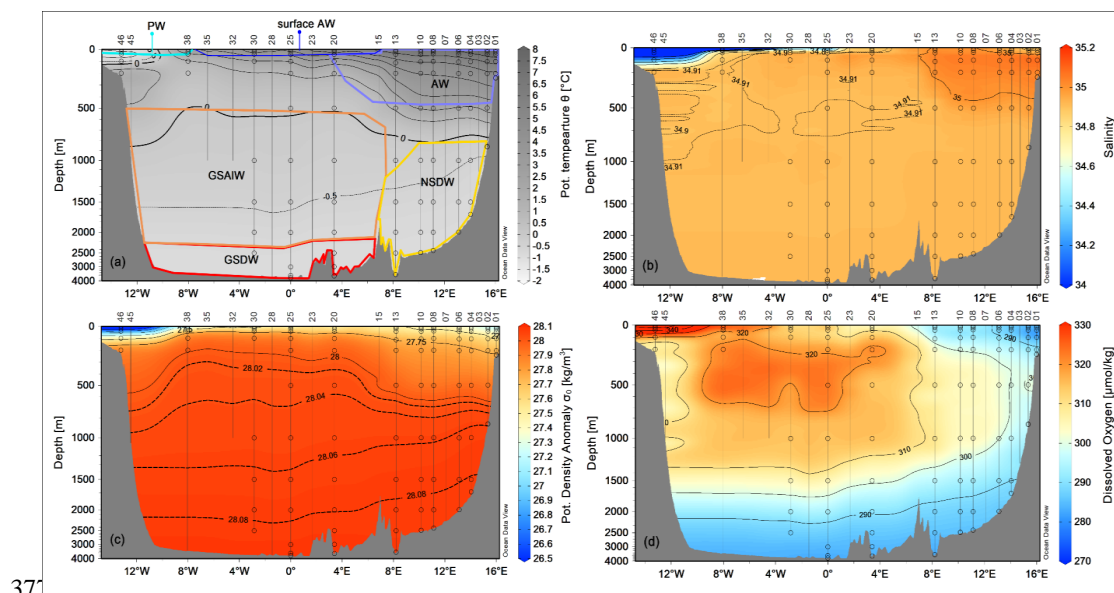
342 **Figure 2 - Upper panels:** satellite images of the Greenland Sea and the Fram Strait in March and September 2021
343 (MODIS Corrected Reflectance Imagery, source NASA). **Bottom panels:** April and September mark the annual
344 maximum and minimum sea ice extension in the Fram Strait (source: Norwegian Polar Institute, 2024, Environmental
345 monitoring of Svalbard and Jan Mayen (MOSJ). URL: [https://mosj.no/en/indikator/climate/ocean/sea-ice-extent-in-](https://mosj.no/en/indikator/climate/ocean/sea-ice-extent-in-the-barents-sea-and-fram-strait/)
346 [the-barents-sea-and-fram-strait/](https://mosj.no/en/indikator/climate/ocean/sea-ice-extent-in-the-barents-sea-and-fram-strait/)). The yellow vertical bar indicates the year 2021.

347 3.1 Physical Oceanography: thermohaline properties distribution

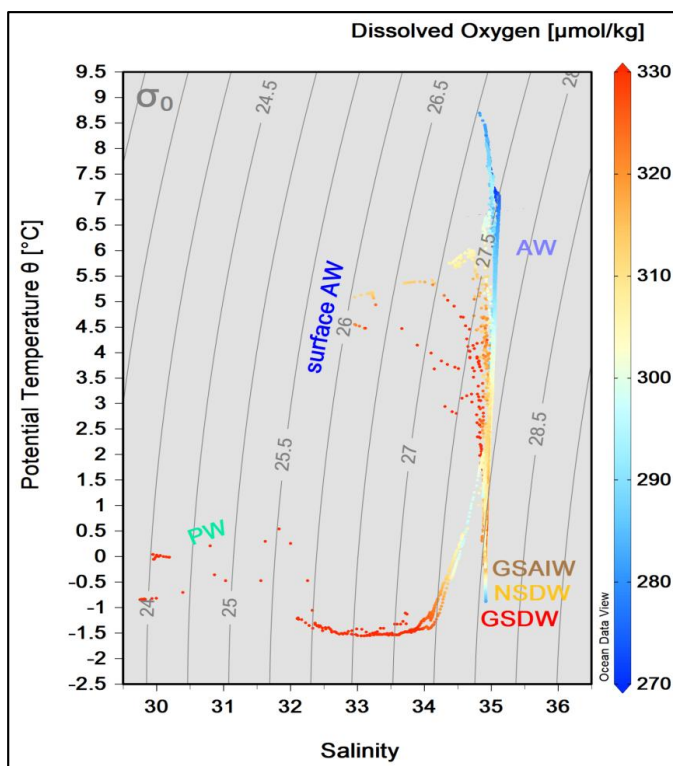
348 We grouped our data according to the definition of main water masses from Rudels et al. (1999)
349 and Wang et al. (2021) and adjusted them to include most of our data. Due to some data gaps, it
350 was not possible to define all relevant water masses in this area more precisely. Along the zonal
351 transect at 75°N, the ocean temperature shows a very pronounced horizontal gradient, with typical
352 values of AW ($\theta > 3.0$ °C, $S > 35$) in the uppermost 500 m of the water column on the eastern side
353 (Fig. 3). At the surface, the AW has temperatures between 4.5 °C and 9.0 °C (Fig. 4). The AW
354 extends to the west and gradually becomes shallower, so that from station 20 to station 35 it only
355 occupies the uppermost 50-80 metres. In contrast, the surface layer on the western side, from station
356 38 to 46, has a thin (about 40-80 m) layer of Polar Water (PW) with temperature and salinity values
357 that are typical of sea ice meltwater ($\theta < 0$ °C, $S \leq 33$). The intermediate zone between 100 m and
358 500 m is largely occupied by mixed water and we refer to it as the transition layer. The deep layer
359 below 500 m depth is occupied by Greenland Sea Arctic Intermediate Water (GSAIW, $-0.9 < \theta < 0$
360 °C, $S \sim 34.9$), Greenland Sea Deep Water (GSDW, $\theta < -1$ °C, $S < 34.9$) in the central and
361 westernmost part, respectively, and Norwegian Sea Deep Water (NSDW, $\theta \sim -1.0$ °C, $S \sim 34.9$) in



362 the easternmost part of the section. We find that the deep layer below 500 m has homogeneous
363 thermohaline properties, with a slightly pronounced difference at the easternmost edge where the
364 NSDW flows northwards. Isotherm at 0 °C and the overall distribution of isopycnals (Fig. 3 a, c)
365 show a classic dome shape with an upwelling in the central part caused by the effect of the GSG,
366 which tends to lift the intermediate water towards the surface due to its cyclonic (i.e., anticlockwise)
367 sense of rotation. In addition, we are certain that the strong horizontal shear and local meteorological
368 conditions can induce the formation of several mesoscale structures (i.e., eddies, hardly shown by
369 our spatial resolution ranging from about 20 km (along the sides) to 40-60 km (in the centre of the
370 transect). They can change the internal distribution and even trap nutrients and other chemical-
371 biological properties. The dissolved oxygen values show a higher oxygen enrichment ($> 350 \mu\text{mol}$
372 kg^{-1}) in the intermediate layer between stations 15 and 38 (Fig. 3d), while the maximum values are
373 found in the upper layer near the Greenland coasts, where the PW flows southwards. In contrast,
374 lower oxygen values ($< 300 \mu\text{mol kg}^{-1}$) are found below 1500 m depth and in the westernmost part
375 of the section where AW and NSDW occur (Fig. 3d). Overall, θ spans from 1.5 °C to almost 9 °C,
376 while S spans from 30 (melting waters) to 35 (AW, Fig. 4).



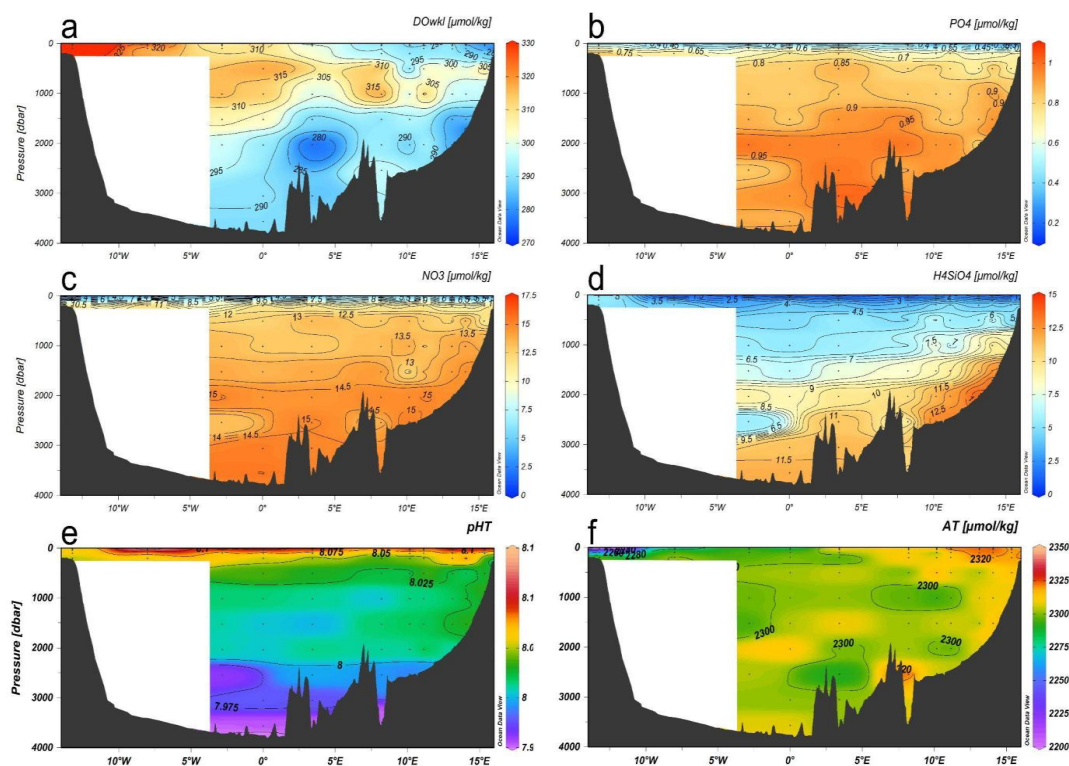
378 **Figure 3** - Vertical distribution of (a) potential temperature (°C), (b) salinity, (c) potential density anomaly (kg m^{-3}), and
379 (d) dissolved oxygen ($\mu\text{mol kg}^{-1}$) along the zonal transect at 75° N in September 2021. The empty dots indicate the
380 sampling points of the Niskin bottles. Panel a show also the distribution of principal water masses according to their core
381 values [AW - Atlantic Water; GSAIW - Greenland Sea Arctic Intermediate water; NSDW - Norwegian Sea Deep Water;
382 GSDW - Greenland Sea Deep Water; PW - Polar Water or Melting Water].
383



384
385 **Figure 4** - θ/σ_t diagram from the CTD data collected along the 75 °N section, during the LB21 cruise in September
386 2021. The colorbar on the right-hand side refers to the values for dissolved oxygen concentration ($\mu\text{mol kg}^{-1}$). [For
387 water masses acronyms see caption of figure 3].

388 3.2 Biogeochemistry

389 Along the entire transect, except for the two edges, the seasonal warming in summer had created a
390 well-stratified upper layer about 30-50 metres deep. At the surface, the central Greenland Sea
391 appears to be almost nutrient poor (Fig. 5). The western side of the transect is characterised by
392 higher concentrations of phosphate and silicate, good indicators of the upper halocline of Arctic
393 surface water along the Greenland slope, whereas nitrate concentrations are very low. At depth,
394 NSDW and GSDW (see Fig. 3, 5) were enriched with silicate.



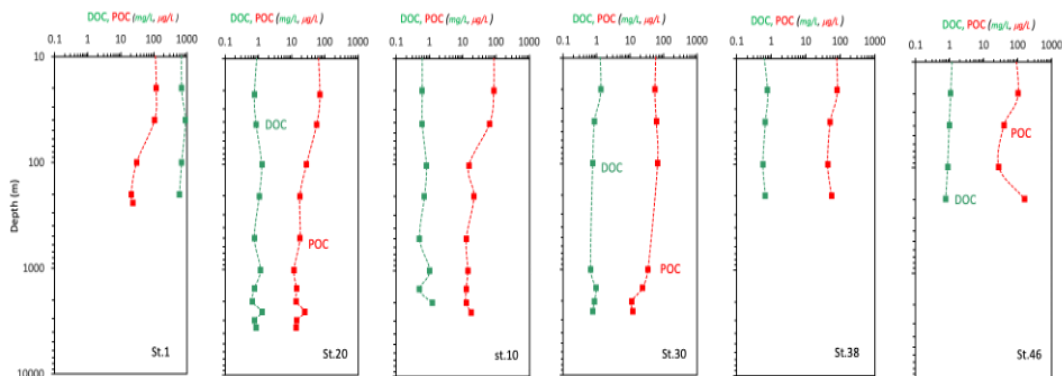
395
396 **Figure 5** - Vertical distribution of (a) dissolved oxygen concentration ($\mu\text{mol/kg}$), (b, c, d) nutrients concentration
397 ($\mu\text{mol/kg}$), (e) pH_T , and (f) Total Alkalinity ($\mu\text{mol/kg}$) along the zonal transect at 75°N during the LB21 cruise in
398 September 2021. Data are obtained from the laboratory analyses on water samples.
399

400 A marked vertical gradient is found along the entire transect with higher pH_T values (up to 8.227,
401 Fig. 5e) in the photic layer ($< 100\text{ m}$ depth) decreasing with increasing depth and reaching the lowest
402 values (7.946-7.997) in the deep layer of the Greenland Sea, presumably due to the degradation of
403 settling organic matter. High total alkalinity values (Fig. 5f) are found on the easternmost side where
404 the AW and NSDW flow northwards. The highest values (A_T up to $2320\text{--}2348\ \mu\text{mol kg}^{-1}$) are found
405 in the higher salinity AW and particularly in the photic layer also due to the contribution of
406 photosynthetic activity. The lowest values are instead associated with fresh Polar Water found at
407 the surface on the westernmost part of the section.
408

409 At the surface layer, a high variability in the rates of respiratory activity and organic matter pool
410 (POC and DOC) was observed (Fig. 6); a decreasing trend up to 1000 m and an interesting increase
411 towards greater depths characterised the vertical profiles of both respiratory activity and DOC. POC
412 concentrations ranged from $11.2\ \mu\text{g C L}^{-1}$ (St 30, at 2002 m depth; $0.93\ \mu\text{M C}$) to $160\ \mu\text{g C L}^{-1}$ (St
413 46, at 198 m depth; $13.3\ \mu\text{M C}$). A greater variability with depth was observed (Coefficient of
414 Variation higher than 65). The highest values were generally found at the surface and within the
415 20–40 m depth interval. The highest mean concentrations were measured at station 46 (mean 80.5
416 $\pm 53.4\ \mu\text{g C L}^{-1}$), mean values at stations 1, 38 and 30 (67.2 ± 46.8 ; 60.0 ± 15.3 and $41.0 \pm 23.1\ \mu\text{g}$
417 C L^{-1} , respectively) and the lowest at stations 10 and 20 (34.1 ± 31.0 and $28.2 \pm 20.5\ \mu\text{g C L}^{-1}$,
418 respectively). DOC showed classic vertical profiles, with the highest concentrations ($1.22\ \text{mg C L}^{-1}$

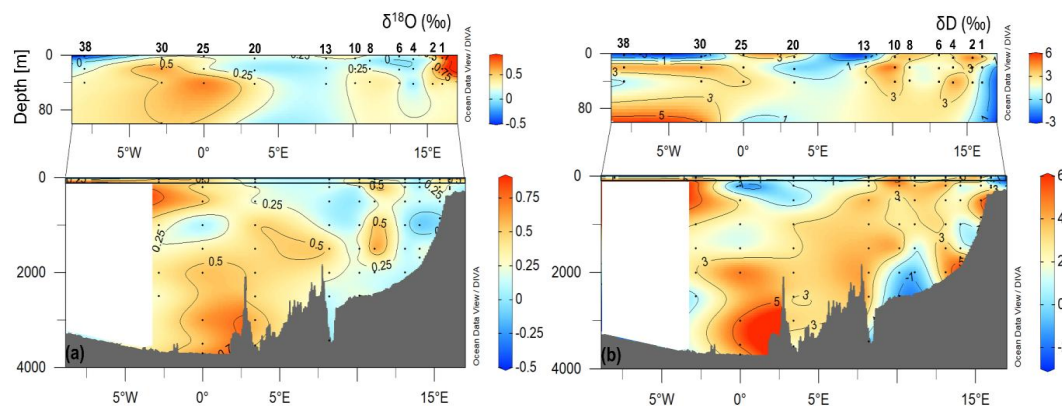


419 ¹; 101.7 $\mu\text{M C}$) at station 30 at 20 m depth and a decrease to a minimum of 0.5 mg C L^{-1} (41.7 $\mu\text{M C}$)
 420 C) at station 10 at 499 m depth. Between 200 and 1000 m depth, the values remained low (mean
 421 $0.83 \pm 0.22 \text{ mg C L}^{-1}$; $69.2 \pm 18.3 \mu\text{M C}$), while a slight increase was observed in the bottom water,
 422 particularly at stations 20 and 10 (Fig. 6).



423
 424 **Figure 6** - Vertical profiles of Dissolved Organic Carbon (DOC, mg L^{-1}) and Particulate Organic Carbon (POC, $\mu\text{g L}^{-1}$) concentrations; Data are represented in natural log (\ln) scale.
 425

426 The isotope values in the total of 96 analysed samples range from -0.43 to 0.8‰ for $\delta^{18}\text{O}$ and from
 427 -2.51 to 5.36‰ for δD . Along the transect, a gradient from west to east can be seen in the surface
 428 waters, with lower values for $\delta^{18}\text{O}$ and δD on the westernmost side (Fig. 7). The lowest values at
 429 the surface in the westernmost part of the section could be related to fresh PW, while the higher
 430 values in the easternmost part could be related to northward flowing AW. At depths between 500
 431 and 1000 m, isotope values drop to a relative minimum, while maxima occur near the bottom at
 432 stations 20 and 25, where GSDW is identified. In addition, a minimum is observed at depth at
 433 stations 8 and 10, in an area occupied by NSDW.



434
 435 **Figure 7** - Vertical distribution of $\delta^{18}\text{O}$ (a) and δD (b) along the zonal transect at 75° N during the LB21 cruise in
 436 September 2021.

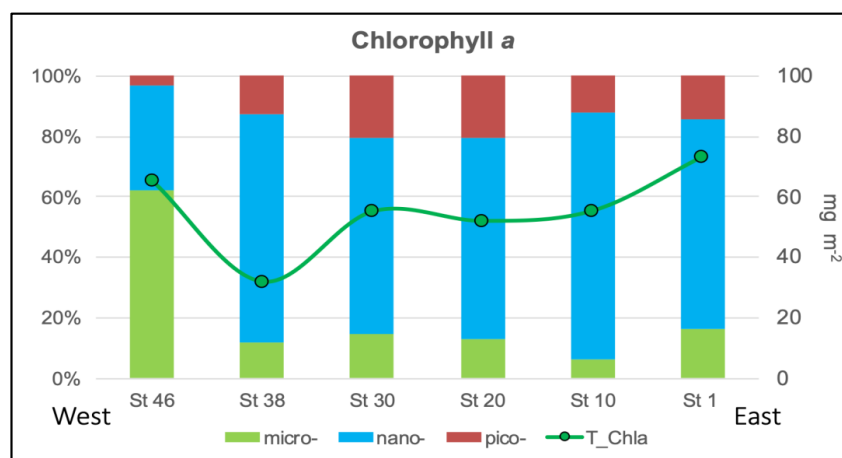


437 3.3 Phytoplankton

438 3.3.1 Total and size-fractionated chlorophyll *a* (chl-*a*)

439 Integrated total chl-*a* in the euphotic layer of the water column (0-100 m) averages 55.4 mg m⁻²
440 while the highest concentrations (73.1 mg m⁻²) were found in the stations located at the ends of the
441 transect (65.3 mg m⁻²) close to the continental shelf (Fig. 8) with the maximum at the easternmost
442 station (st. 46). Overall, the concentration of chl-*a* ranges between 0.20 mg m⁻³ (St.1, 100 m) and
443 2.90 mg m⁻³ (St.1, 20 m) with a mean value of 0.63 ± 0.64 mg m⁻³. Degraded pigments (phaeo) are
444 around 40 % with respect to chl-*a*. The size spectrum of the phytoplankton community biomass
445 along the water column, shows different percentage contributions to the total with 65% for the nano-
446 phytoplankton, 21% for the micro-fraction and 14% for the pico-phytoplankton (Fig. 8). Exception
447 to this composition is observed in the westernmost station (st. 46) where the micro-fraction
448 dominates, replacing the nano-phytoplankton.

449



450

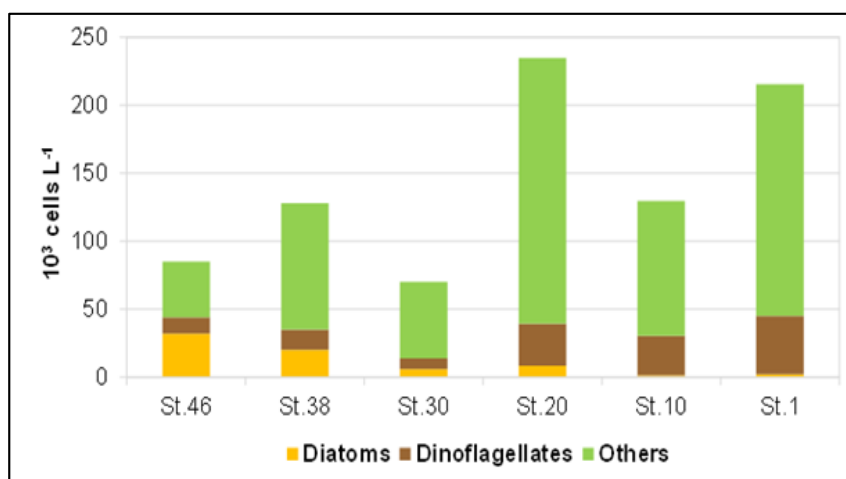
451 **Figure 8** - Integrated total chl-*a* concentration (0-100 m depth) at the stations along the 75°N zonal transect (green line)
452 with the percentage of contribution of micro- nano- and pico-phytoplankton size-fractions (histogram).

453 3.3.2 Phytoplankton composition and abundances

454 The phytoplankton analyses do not reveal a clear pattern along the transect, although some
455 differences in abundance and composition were observed. The integrated abundances of
456 phytoplankton, ranging from 7.00 (st. 30) to 23.48 x 10⁴ cells L⁻¹ (st. 20), are higher at the
457 easternmost stations than at the westernmost ones (on average 19.33 x 10⁴ cells L⁻¹ at stations 1, 10,
458 20 and 9.44 x 10⁴ cells L⁻¹ at stations 30, 38, 46, see Fig. 9). This is mainly due to a more even
459 vertical distribution of abundance at the eastern stations. In contrast, the westernmost stations have
460 even higher phytoplankton abundances, but limited to subsurface maxima, like 50.40 x 10⁴ cells L⁻¹
461 at 38 m at station 20, while abundances in the rest of the water column are very low. The
462 phytoplankton community along the transect is characterised by the dominance of the flagellate
463 group (70% of the total phytoplankton), mainly represented by small (< 10 μm) forms with uncertain
464 taxonomic identification (on average, 61%). Diatoms (on average, 9% of the total phytoplankton)
465 are present in very low abundances in the easternmost stations (on average, 0.43 x 10⁴ cells L⁻¹ at
466 stations 1, 10, 20, 30), while higher values were recorded in the two westernmost stations 38 and
467 46 (on average, 3.24 x 10⁴ cells L⁻¹). Finally, dinoflagellates accounted for an average of 21% of



468 the total phytoplankton, with higher abundances occurring in the easternmost stations than in the
469 westernmost stations (3.32×10^4 cells L^{-1} and 1.42×10^4 cells L^{-1} , respectively).



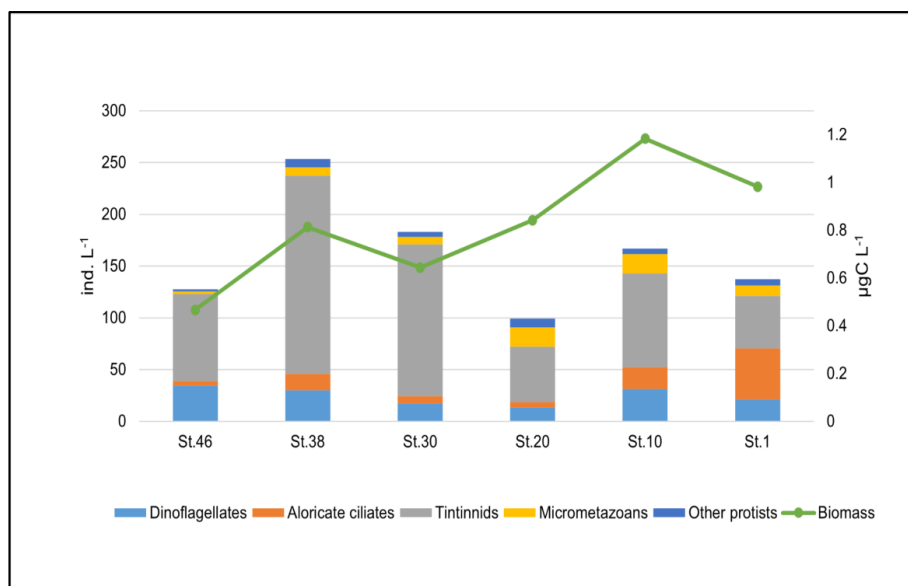
470

471 **Figure 9** - Integrated contribution of the main phytoplankton groups (diatoms, dinoflagellates, and others) to
472 phytoplankton abundance at sampled stations along the 75°N transect.

473 3.4 Zooplankton

474 3.4.1 Microzooplankton abundance and biomass

475 The MZP abundance in the study area varies between 721.5 ind. L^{-1} (St. 38, at 0 m) and 6.25 ind. L^{-1}
476 (St. 20, at 3500 m). The carbon content shows higher values at the surface with a maximum value
477 of 1.7 $\mu g C L^{-1}$ (St. 38, 0 m) and a minimum of 0.01 $\mu g C L^{-1}$ at 2520 m depth (St. 10). The vertical
478 distribution of organisms, based on their abundance along the water column, shows higher
479 abundances in the first 200 m, compared to the zone > 200 m. In particular, the integrated abundance
480 of MZP in the upper layer reaches its maximum at St. 38, mainly due to the higher presence of
481 tintinnids, while the lowest values are found at St. 20, in the centre of the transect (Fig. 10). The
482 highest carbon content is recorded at St. 10, which is due to the high abundance of other protists
483 and micrometazoans (Fig. 10). Tintinnids are the most abundant taxa in the study area, followed by
484 heterotrophic dinoflagellates and aloricate ciliates (Fig. 10).

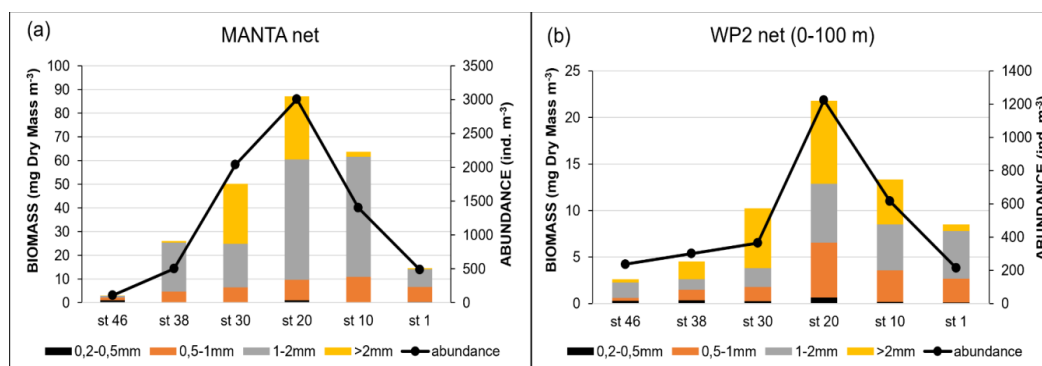


485

486 **Figure 10** - Integrated values of abundance (ind. L⁻¹) and biomass (µgC L⁻¹) of microzooplankton in the upper layer (<
487 200 m depth).

488 3.4.2 Mesozooplankton biomass and abundance

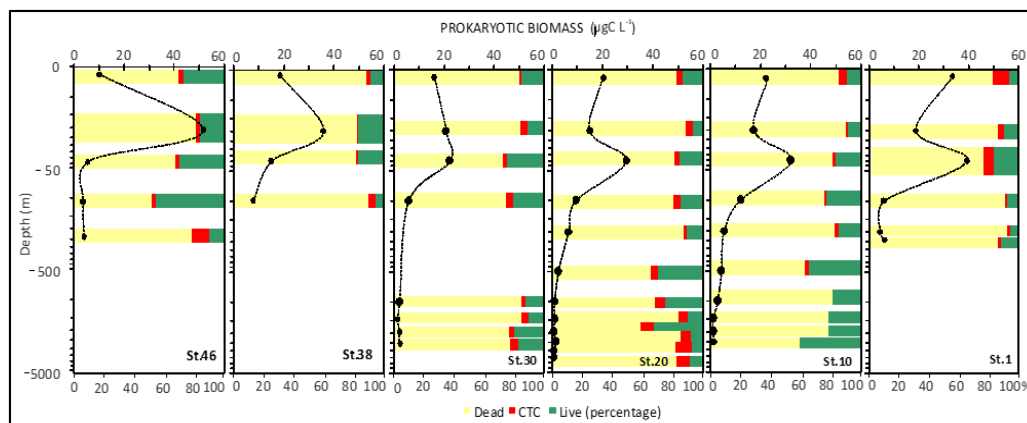
489 Biomass and abundance of mesozooplankton have the same distribution along the transect both at
490 the surface (ca. 20 cm depth, Fig. 11a) and in the upper layer (0-100 m depth, Fig. 11b), with the
491 highest values found in the central part of the transect (St. 20). Nevertheless, the surface samples
492 are richer in organisms than those collected in the water column (mean abundance: Manta net: 1257
493 ± 1110 ind. m⁻³; WP2 net: 492 ± 387 ind. m⁻³), which also corresponds to a higher biomass (mean
494 biomass: Manta net: 41 ± 32 mgDM m⁻³; WP2 net: 10 ± 7 mgDM m⁻³). Overall, organisms 1-2 mm
495 in size account for 61 % of the mesozooplanktonic biomass in the surface waters and are the most
496 abundant at almost all stations (Fig. 11a), while in the samples collected with the WP2 net, the
497 biomass fractions consisting of organisms 1-2 mm and > 2 mm in size were the most abundant,
498 accounting for 35 and 38 % of the total biomass, respectively (Fig. 11b). Copepods are the most
499 abundant taxon both at the surface and in the upper layer (97 % and 94 % of the total
500 mesozooplankton abundance, respectively), mainly represented by the genus *Calanus*.
501 Chaetognaths, although much less abundant than copepods, are found along the entire transect both
502 at the surface and in the upper layer, being most numerous at stations 10, 20, and 30. Molluscs are
503 almost absent in the surface water and are mainly found in the water column at the eastern stations
504 of the transect (St. 1 and St.10).



505
 506 **Figure 11** - Biomass and abundance of mesozooplankton: (a) Manta net sampling at surface and (b) WP2 net sampling
 507 in the 0-100 m layer.

508 3.5 Microbial compartment: abundance, biomass, and activities

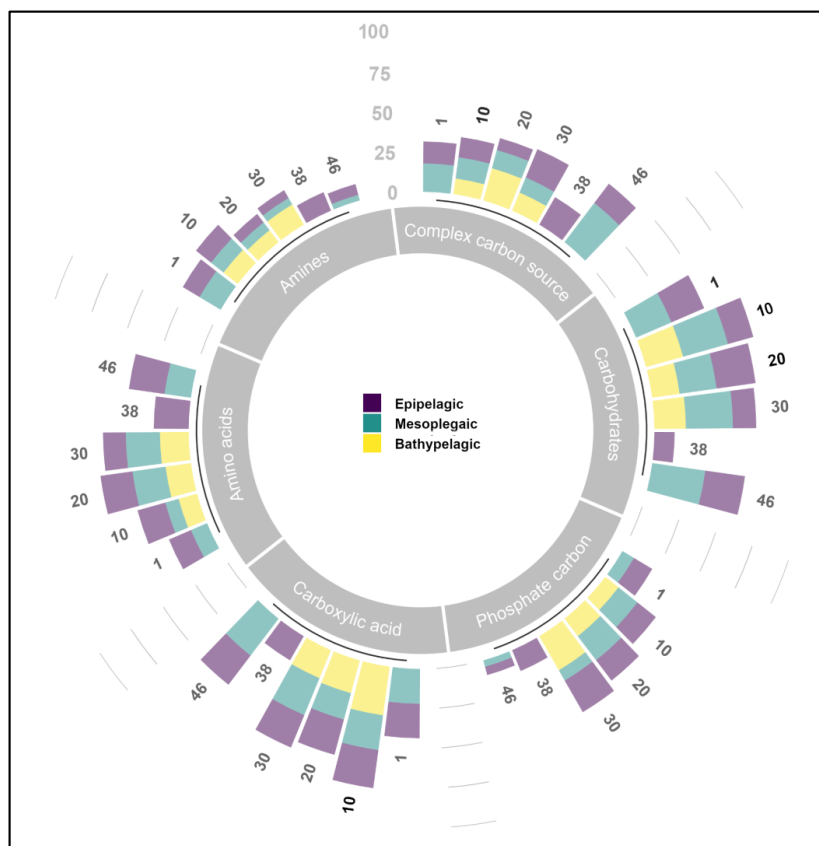
509 The abundance of prokaryotes is high in the photic (0-100 m depth) layer (range: 5.57 to 11.3×10^5 cells m^{-3}) and decreases with depth. The highest values are measured at stations 20 and 1. From
 510 100 to 1000 m depth, the abundance ranges from 1.75 to 3.21×10^5 cells m^{-3} and from 0.53 to 0.64×10^5 cells m^{-3} at greater depths. The cell volume ranges from 0.049 to $0.098 \mu m^3$, with a mean
 511 value of $0.072 \pm 0.018 \mu m^3$. In the photic and aphotic layers, the cell volumes vary in a similar
 512 range ($0.08 \pm 0.02 \mu m^3$). The highest volumes at great depths characterise stations 30 and 10, where
 513 large, curved rods are observed. Apart from stations 30 and 10, the data show a similar vertical
 514 profile in the size distribution. The highest percentage of live cells (about 33%) is observed at
 515 station 46 in the photic layer. However, peaks are also found in the deeper layers. The number of
 516 respiring cells (CTC+) is in the order of 104 cells ml^{-1} . Variability between the layers is observed
 517 at all stations. In general, the high proportion of respiring cells below 100 m depth is observed
 518 at stations 46, 30 and 20. Conversely, the higher percentages are found in the photic layer at stations
 519 St. 10 and 1 (Fig. 12).
 520
 521



522
 523 **Figure 12** - Vertical profiles of prokaryotic biomass, viable and dead cells (Live/Dead) and respiring cells (CTC); Data
 524 on y axis are represented in natural log (h) scale.



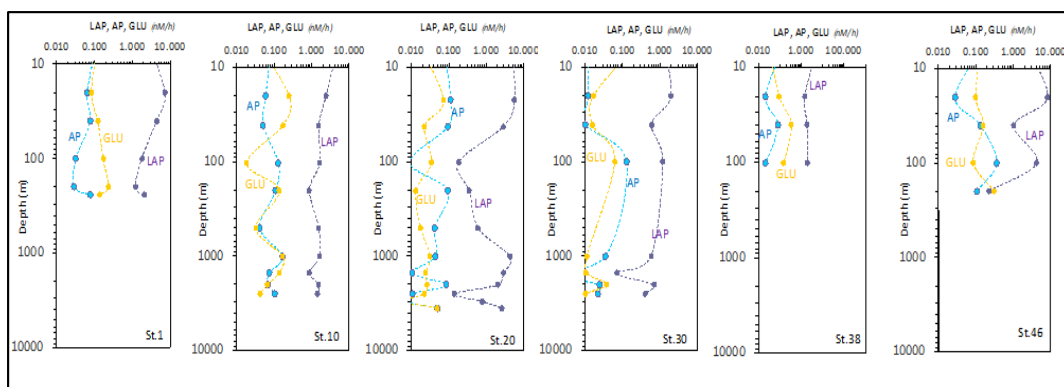
525 Overall, the average percentages of carbon source utilisation determined by Biolog Ecoplates show
526 that carbohydrates and carboxylic acids were well-utilised polymers at each station and in each
527 layer. Especially in the aphotic layer, the percentage utilisation is highest at most stations. Complex
528 carbon sources and phosphate carbon are utilised at similar percentages throughout the water
529 column; conversely, amino acids are preferentially utilised in the aphotic layer. Amines are only
530 little used (Fig. 13).



531

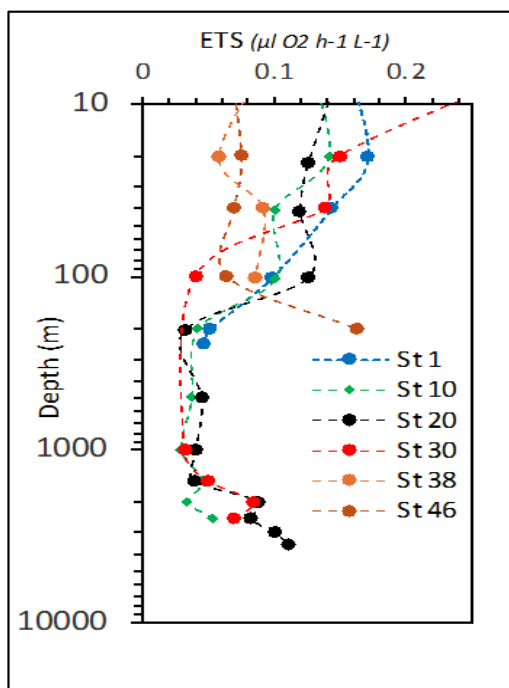
532 **Figure 13** - Carbon substrate utilisation (as percentage of the total) determined in the epi-, meso-, and bathypelagic
533 layers.

534 Enzymatic activity measurements yield values of LAP, GLU and AP ranging from 0.072 to 8.08
535 nM h^{-1} , from 0.007 to 0.35 nM h^{-1} and from 0.001 to 0.36 nM h^{-1} respectively (Fig. 14). Total
536 enzymatic patterns depict vertical trends generally decreasing from surface towards deep layers,
537 with some hot spots of metabolic activity at 20-40 m and in the aphotic layer. LAP activity peaks
538 at the lateral ends of the transect as well as at St. 20. AP and GLU decrease from the Western
539 (Greenland) side moving towards St 20, then increase again towards the Eastern side (St. 10) of
540 the transect.



541
542 **Figure 14** - Vertical profiles of the enzymatic activity rates measured at the sampled stations (LAP, leucine
543 aminopeptidase; AP, alkaline phosphatase; GLU, beta glucosidase). Data are represented in natural log (*ln*) scale.
544

545 The respiration rates (ETS) range from 0.0290 to 0.329 $\mu\text{L O}_2 \text{ h}^{-1} \text{ L}^{-1}$ (Fig. 15). The respiratory
546 activity values generally decrease from the surface to 1000 m depth and then increase in the deeper
547 layer. A high value of respiratory activity was also determined in the deepest sample of St. 46.



548
549 **Figure 15** - Vertical profiles of Electron Transport System (ETS) respiratory activity. Data on the y axis are
550 represented in natural log (*ln*) scale.
551



552 4 **Summary and conclusions**

553 Here we present the main data and results of the multidisciplinary oceanographic campaign carried
554 out between 29 August and 14 September 2021 on board the Italian icebreaker Laura Bassi in the
555 Greenland Sea (along the 75° N latitude section) as part of the Italian project CASSANDRA, funded
556 by the Italian Ministry of Research in the framework of the Italian Arctic Programme. The
557 Greenland Sea, in the north Atlantic, is a region of deep ocean convection that contributes to the
558 AMOC and the exchange of water masses between the Atlantic and Arctic Oceans. On its
559 easternmost side, it is dominated by the presence of AW, while on the westernmost side, by the
560 presence of Polar waters. Both large scale patterns, local meteorological conditions, and ice extent
561 can influence physical and biogeochemical properties. Different phases of the North Atlantic
562 Oscillation index (NAO, i.e., atmospheric pressure difference between the Azores high and the
563 subpolar low at sea level) can modulate basin-wide changes in the intensity and position of the
564 North Atlantic jet stream and storm track, as well as influence patterns of zonal and meridional heat
565 and moisture transport, which in turn can affect temperature and precipitation patterns over the
566 Arctic and sub-Arctic regions. Increasingly positive phases of the NAO are associated with
567 increased AW inflow, as was the case in the late 1980s/early 1990s (Dickson et al., 2000). The
568 winter of 2020/2021, which preceded the cruise, had a slightly negative NAO index (-0.72), after
569 two years of predominantly positive values. A negative NAO means weaker westerly winds in the
570 mid-latitude regions in terms of climatology and stronger winds in the North Atlantic west of
571 Iceland. Sea ice in the Fram Strait fluctuates from year to year. The lowest extent in September was
572 recorded exactly in 2021, the highest in 1987. In the long term, the regions of the Norwegian Sea
573 and the Fram Strait experienced a drop in temperature from 2018 to 2020, which rose again in 2021.
574 Instead, a strong freshening phase set in after 2013, which is continuing. Continuous warming was
575 also observed in the deep-water layer of the Greenland Sea at a depth of 3000 metres. In particular,
576 the GSDW temperature shows a relatively steady increase from -1.18 °C to -0.86 °C between 1993
577 and 2021 (ICES Report on Ocean Climate 2021, available at [https://ices-
578 library.figshare.com/articles/report/ICES_Report_on_Ocean_Climate_2021/24755574?file=43769571](https://ices-library.figshare.com/articles/report/ICES_Report_on_Ocean_Climate_2021/24755574?file=43769571)). Our
579 measurements report temperature values of about -0.9 °C for the GSDW. Relatively warm and
580 saline Atlantic Water (AW, $\theta > 3.0^{\circ}\text{C}$, S about 35), with highest A_T concentrations, dominates on
581 the eastern side in the upper 500 m with surface temperatures of 4.5–9.0 °C. A dome-shaped
582 isotherm distribution indicates upwelling from the Greenland Sea Gyre, while several mesoscale
583 structures such as eddies seem to be responsible for the large spatial variability in the upper layer.
584 At the surface, the central Greenland Sea is almost nutrient poor. On the western side, however,
585 higher phosphate and silicate values are good indicators for the upper halocline of the Arctic surface
586 water along the Greenland slope. Nitrate levels remained very low there. The deep waters NSDW
587 and GSDW, presented the lowest pH_T values and the highest enrichment of silicate. Phytoplankton
588 biomass along the euphotic water column, expressed as chl-*a*, showed a quali-quantitative
589 difference between the central-eastern and western sectors with greater abundances at the extremes
590 of the transect. The dimensional structure of the phytoplankton community characterizes the PW
591 with a predominance of the micro-phytoplankton fraction that almost entirely replaces the nano-
592 phytoplankton fraction, more abundant in the AW, even in the front station between these two water
593 masses. The plankton communities were analysed with more detail in the upper layer (0-100 m),
594 where the phytoplankton and zooplankton diversity reflected the different water masses (AW and
595 PW). Diatoms increased at the western stations affected by PW, while dinoflagellates and small



596 flagellates were more abundant at the eastern stations affected by AW. The higher MZP abundance
597 was recorded at St. 38, where the layer below 30-40 m depth was still occupied by AW, while the
598 surface layer was affected by PW. The MZP abundance and biomass decreased drastically in the
599 presence of cold PW on the Greenland slope. Micrometazoans and aloricate ciliates increased
600 towards the easternmost side of the section, where the stations were characterised by higher
601 temperatures. Copepods of the genus *Calanus* were the main taxa observed, but the structure of the
602 mesozooplankton communities changed during the transect and polar taxa increased westwards.
603 The $\delta^{18}\text{O}$ and δD isotope ratios indicate the influence of freshwater at the surface level near the
604 Greenland shelf. We also highlight a marked difference in $\delta^{18}\text{O}$ and δD isotope ratios between
605 GSDW and NSDW, which occupies the bottom region of the studied area, with NSDW showing
606 lighter values compared to GSDW. Prokaryotic abundance and microbial enzymes generally
607 depicted vertical decreasing trends with peaks of cells and activity recorded at station 20 as well as
608 at the ends of the transect. While living cells prevailed at station 46 in the photic layer, actively
609 respiring cells were quite variable in their distribution. Large, curved rods were found at stations 30
610 and 10. A high utilization of carbohydrates and carboxylic acids regardless of the examined station
611 or depth characterized the microbial community metabolism. Amino acids were actively
612 metabolised in the aphotic layer, while no differences were found in the utilization of complex
613 carbon sources and phosphate carbon compounds along the water column.

614 This study emphasises the significant spatial and vertical variability of water properties, nutrient
615 distribution and biological communities caused by local and seasonal oceanographic dynamics in a
616 region characterised by a strong exchange of water masses between the Arctic and Atlantic Oceans
617 and a major influence of atmospheric teleconnections between the polar and subpolar regions.

618 **5 Data availability**

619 Data presented here are available through the repository Italian Arctic Data Center (IADC), at the
620 following links: CTD casts, available at <https://doi.datacite.org/doi/10.71761%2F082c3ca-40bf-42b1-a61a-7b3697ab2c5a> (Bensi et al., 2024). Physical, biological, and biogeochemical analyses
622 on water samples from Niskin bottles available at
623 <https://doi.datacite.org/doi/10.71761%2Ff7474404-3331-43e5-883b-25755e94956d> (Azzaro et
624 al., 2024). Satellite data used in the work are freely available at
625 <https://worldview.earthdata.nasa.gov/>. Data on sea ice extension are available at
626 <https://mosj.no/en/indikator/climate/ocean/sea-ice-extent-in-the-barents-sea-and-fram-strait/>.

627 **Declaration of Competing Interest**

628 The authors declare that they have no known competing financial interests or personal relationships
629 that could have appeared to influence the work reported in this paper.

630 **Acknowledgements**

631 The field activities carried out on board the icebreaker Laura Bassi were partly funded by the Italian
632 Ministry of University and Research through the Italian Arctic Research Programme
633 (<https://www.programmaricercaartico.it/>), the National Institute of Oceanography and Applied
634 Geophysics (OGS) and the National Research Council (CNR). The research was conducted as part
635 of the project "AdvanCing knowledge on the present Arctic Ocean by chemical-physical,



636 biogeochemical and biological obServAtioNs to preDict the futuRe chAnges" (CASSANDRA),
637 which was funded by the Italian Arctic Research Programme (CASSANDRA project;
638 PRA21_0001). This study was supported by the Synoptic Arctic Survey (SAS) – an international
639 research programme that coordinates the data collection of essential ocean variables measured
640 during Arctic research cruises. SAS is partly funded by the European Union's Horizon 2020
641 research and innovation programme through the Arctic PASSION project under the grant agreement
642 10100347. We would also like to thank Lidia Urbini, Paolo Mansutti, Leonardo Langone, Patrizia
643 Giordano, Warren Cairns, Matteo Feltracco, the entire technical staff of the OGS, the captain and
644 crew of the Laura Bassi for their support during the data collection. We also thank Alenka Goruppi
645 and Giulia Peloso (OGS, Trieste, Italy) for their help in processing the zooplankton data and Nives
646 Ogrinc (Jožef Stefan Institute Ljubljana, Slovenia) for the analyses of $\delta^{13}\text{C}$ -DIC.

647 **Author contribution**

648 M.B., M.A. and G.Ci. conceived and wrote the main part of the article. M.B., M.A., G.Ci., M.G.,
649 V.K., C.R., M.M., T.D., F.R., M.K., A.L.G., V.T., E.P., A.d.O., D.B., F.C., A.C.R., M.P., G.Ca.,
650 G.M., C.T., L.P. F.S., F.D., C.C. contributed to the collection and/or processing of the data,
651 preparation of figures, and to the discussion of the results. M.A. led the CASSANDRA project. All
652 authors have contributed to the preparation and revision of the final version of the manuscript.



653 **References**

654 Ahme, A., Von Jackowski, A., McPherson, R. A., Wolf, K. K. E., Hoppmann, M., Neuhaus, S. and
655 John, U.: Winners and Losers of Atlantification: The Degree of Ocean Warming Affects the
656 Structure of Arctic Microbial Communities, *Genes*, 14, 623.
657 <https://doi.org/10.3390/genes14030623>, 2023.

658 Andersen, P., and Throndsen, J.: Estimating cell numbers, in: *Manual on Harmful Marine*
659 *Microalgae*, edited by: Hallegraeff, G. M., Anderson, D. M., and Cembella, A., Monographs on
660 *Oceanographic Methodology*, Unesco Publishing, Paris, France, 11, 99–130, 2004.

661 Anderson, L. G., Drange, H., Chierici, M., Fransson, A., Johannessen, T., Skjelvan, I., Rey, F.:
662 Annual carbon fluxes in the upper Greenland Sea based on measurements and a box-model
663 approach. *Tellus*, 52B, 1013-1024, 2000.

664 Azzaro, M., Specchiulli, A., Maimone, G., Azzaro, F., Lo Giudice, A., Papale, M., La Ferla, R.,
665 Paranhos, R., Souza Cabral, A., Rappazzo, A. C., et al.: Trophic and Microbial Patterns in the
666 Ross Sea Area (Antarctica): Spatial Variability during the Summer Season. *J. Mar. Sci. Eng.* 10,
667 1666. <https://doi.org/10.3390/jmse10111666>, 2022.

668 Azzaro M., Aliani S., Maimone, G., Decembrini F., Caroppo C., Giglio F., Langone L., Misericocchi
669 S., Cosenza A., Azzaro F., et al.: Short-term dynamics of nutrients, planktonic abundances and
670 microbial respiratory activity in the Arctic Kongsfjorden (Svalbard, Norway). *Polar Biol.* 44,
671 361–378, 2021.

672 Azzaro, M., Bensi, M., Civitarese, G., et al. CTD (data from NISKIN Bottles) LB21 ARCTIC Cruise
673 Italian Arctic project CASSANDRA [Data set]. ISP-CNR. [https://doi.org/10.71761/F7474404-
674 3331-43E5-883B-25755E94956D](https://doi.org/10.71761/F7474404-3331-43E5-883B-25755E94956D), 2024.

675 Azzaro, M., La Ferla, R., and Azzaro, F.: Microbial respiration in the aphotic zone of the Ross Sea
676 (Antarctica), *Mar. Chem.*, 99(1), 199-209, <https://doi.org/10.1016/j.marchem.2005.09.011>,
677 2006.

678 Babb, D. G., Galley, R. J., Kirillov, S., Landy, J. C., Howell, S. E. L., Stroeve, J. C., Meier, W.,
679 Ehn, J. K., and Barber, D. G.: The stepwise reduction of multiyear sea ice area in the Arctic
680 Ocean since 1980, *J. Geophys. Res. Oceans*, 128, 10, <https://doi.org/10.1029/2023JC020157>,
681 2023.

682 Beers, J. R., and Stewart, G. L.: Numerical abundance and estimated biomass of microzooplankton,
683 in: *The ecology of the plankton off La Jolla, California, in the period April through September*
684 *1967*, edited by: Strickland, J. D. H., University of California Press, Berkeley, USA, 67–87,
685 1970.

686 Bensi, M., Kovacevic, V., & Mansutti, P.: CTD (DOWNCAST) LB21 ARCTIC Cruise Italian Arctic
687 project CASSANDRA [Data set]. IADC. [https://doi.org/10.71761/C082C3CA-40BF-42B1-
688 A61A-7B3697AB2C5A](https://doi.org/10.71761/C082C3CA-40BF-42B1-A61A-7B3697AB2C5A), 2024.



- 689 Brakstad, A., K. Våge, L. Håvik, and G. W. K. Moore: Water Mass Transformation in the Greenland
690 Sea during the Period 1986–2016. *J. Phys. Oceanogr.*, 49, 121–140, [https://doi.org/10.1175/JPO-](https://doi.org/10.1175/JPO-D-17-0273.1)
691 [D-17-0273.1](https://doi.org/10.1175/JPO-D-17-0273.1), 2019.
- 692 Carmack, E., Polyakov, I., Padman, L., Fer, I., Hunke, E., Hutchings, J., Jackson, J., Kelley, D.,
693 Kwok, R., Layton, C., Melling, H., Perovich, D., Persson, O., Ruddick, B., Timmermans, M.,
694 Toole, J., Ross, T., Vavrus, S., & Winsor, P.: Toward Quantifying the Increasing Role of Oceanic
695 Heat in Sea Ice Loss in the New Arctic. *Bull. of the Am. Met. Society*, 96(12), 2079–2105,
696 <https://doi.org/10.1175/BAMS-D-13-00177.1>, 2015.
- 697 Carpenter, J. H.: The accuracy of the Winkler method for dissolved oxygen analysis. *Limnol.*
698 *Oceanogr.*, 10, 135–140, <https://doi.org/10.4319/lo.1965.10.1.0135>, 1965.
- 699 Carter-Gates, M., Balestreri, C., Thorpe, S. E., Cottier, F., Baylay, A., Bibby, T. S., et al.:
700 Implications of increasing Atlantic influence for Arctic microbial community structure, *Sci.*
701 *Rep.*, 10, 19262, <https://doi.org/10.1038/s41598-020-76293-x>, 2020.
- 702 Caruso, G., La Ferla, R., Azzaro, M., Zoppini, A., Marino, G., Petochi, T., et al.: Microbial
703 assemblages for environmental quality assessment: knowledge, gaps and usefulness in the
704 European Marine Strategy Framework Directive, *Crit. Rev. Microbiol.*, 42, 883–904,
705 <https://doi.org/10.3109/1040841X.2015.1087380>, 2016.
- 706 Caruso, G., Madonia, A., Bonamano, S., Misericocchi, S., Giglio, F., Maimone, G., et al.: Microbial
707 abundance and enzyme activity patterns: response to changing environmental characteristics
708 along a transect in Kongsfjorden (Svalbard Islands), *J. Mar. Sci. Eng.*, 8, 824,
709 <https://doi.org/10.3390/jmse8100824>, 2020.
- 710 Chatterjee, S., Raj, R. P., Bertino, L., Skagseth, Ø., Ravichandran, M., and Johannessen, O. M.: Role
711 of Greenland Sea Gyre Circulation on Atlantic Water Temperature Variability in the Fram Strait,
712 *Geophys. Res. Lett.*, 45, 8399–8406, <https://doi.org/10.1029/2018GL079174>, 2018.
- 713 Clarke, R., Swift, J., Reid, J., and Koltermann, K.: The formation of Greenland Sea Deep Water:
714 double diffusion or deep convection? *Deep Sea Res. Part A, Oceanogr. Res. Pap.*, 37, 1385–1424
715 [https://doi.org/10.1016/0198-0149\(90\)90135-I](https://doi.org/10.1016/0198-0149(90)90135-I), 1990.
- 716 Csapó, H. R., Grabowski, M., and Węśławski J.M.K.: Coming home - Boreal ecosystem claims
717 Atlantic sector of the Arctic, *Sci. Total Environ.*, 771, 144817,
718 <https://doi.org/10.1016/j.scitotenv.2020.144817>, 2021.
- 719 Decembrini, F., Caroppo C., Caruso, G., and Bergamasco, A.: Linking microbial functioning and
720 trophic pathways to mesoscale processes and ecological status in a coastal ecosystem: Gulf of
721 Manfredonia (south Adriatic Sea), *Water*, 13, 1325. <https://doi.org/10.3390/w13091325>, 2021.
- 722 Dickson, R. R., Osborn, T. J., Hurrell, J. W., Meincke, J., Blindheim, J., Adlandsvik, B., et al.: The
723 Arctic Ocean Response to the North Atlantic Oscillation, *J. Climate*, 13, 2671–2696,
724 [https://doi.org/10.1175/1520-0442\(2000\)013<2671:TAORTT>2.0.CO;2](https://doi.org/10.1175/1520-0442(2000)013<2671:TAORTT>2.0.CO;2), 2000.



- 725 de Steur, L., Sumata, H., Divine, D.V., et al. Upper ocean warming and sea ice reduction in the East
726 Greenland Current from 2003 to 2019. *Commun Earth Environ* 4, 261.
727 <https://doi.org/10.1038/s43247-023-00913-3>, 2023.
- 728 Dukhovskoy, D. S., Yashayaev, I., Proshutinsky, A., Bamber, J. L., Bashmachnikov, I. L.,
729 Chassignet, E. P., et al.: Role of Greenland freshwater anomaly in the recent freshening of the
730 subpolar North Atlantic. *J. Geophys. Res. Oceans*, 124, 3333–3360,
731 <https://doi.org/10.1029/2018JC014686>, 2019.
- 732 Edler, L.: Recommendations for marine biological studies in the Baltic Sea. *Phytoplankton and*
733 *chlorophyll. Baltic Mar. Biol.*, 5, 1-37, 1979.
- 734 Fan, H., Borchert, L.F., Brune, S., Koul, V., and Baehr, J.: North Atlantic subpolar gyre provides
735 downstream ocean predictability, *npj Clim. Atmos. Sci.*, 6, 145, [https://doi.org/10.1038/s41612-](https://doi.org/10.1038/s41612-023-00469-1)
736 [023-00469-1](https://doi.org/10.1038/s41612-023-00469-1), 2023.
- 737 Fransner F., Fröb F., Tjiputra J., Goris N., Lauvset S. K., Skjelvan I., Jeansson E., Omar A., Chierici
738 M., Jones E., Fransson A., Ólafsdóttir S. R., Johannessen T., Olsen A.: Acidification of the
739 Nordic Seas, *Biogeosciences*, 19, 979–1012, <https://doi.org/10.5194/bg-19-979-2022>, 2022.
- 740 Grasshoff, K., Kremling, K., and Ehrhardt, M.: *Methods of Seawater Analysis*, Wiley-VCH,
741 Weinheim, 600 pp., 1999.
- 742 Hansen, H. P., and Koroleff, F.: Determination of nutrients, in: *Methods of Seawater Analysis*, 3rd
743 Edn., edited by: Grasshoff, K., Kremling, K., and Ehrhardt, M., Wiley-VCH, Weinheim, 159–
744 228, <https://doi.org/10.1002/9783527613984.ch10>, 1999.
- 745 Hoppe, H. G.: Use of fluorogenic model substrates for extracellular enzyme activity (EEA)
746 measurement of bacteria, 1st edition, In: *Handbook of methods in aquatic microbial ecology*,
747 edited by: Kemp, P. F., Sherr, B. F., Sherr, E. B., and Cole, J. J., Lewis Publisher, Boca Raton,
748 FL-USA, 423-432, <https://doi.org/10.1201/9780203752746>, 1993.
- 749 Ingrosso, G., Giani, M., Comici, C., Kralj, M., Piacentino, S., De Vittor, C., Del Negro, P.: Drivers
750 of the carbonate system seasonal variations in a Mediterranean gulf. *Estuar. Coast. Shelf Sci.*
751 168, 58-70, <https://doi.org/10.1016/j.ecss.2015.11.001>, 2016a.
- 752 Ingrosso, G., Giani, M., Cibic, T., Karuza, A., Kralj, M., Del Negro, P.: Carbonate chemistry
753 dynamics and biological processes along a river–sea gradient (Gulf of Trieste, northern Adriatic
754 Sea). *J.Mar. Syst.* 155, 35–49. <http://dx.doi.org/10.1016/j.jmarsys.2015.10.013>, 2016b.
- 755 Ingvaldsen, R.B., Assmann, K.M., Primicerio, R., et al.: Physical manifestations and ecological
756 implications of Arctic Atlantification. *Nat Rev Earth Environ* 2, 874–889.
757 <https://doi.org/10.1038/s43017-021-00228-x>, 2021.
- 758 La Ferla, R., Maimone, G., Azzaro, M., Conversano, F., Brunet, C., Cabral, A.S., Paranhos, R.:
759 Vertical distribution of the prokaryotic cell size in the Mediterranean Sea. *Helgol. Mar. Res.* 66,
760 635–650. <https://doi.org/10.1007/s10152-012-0297-0>, 2012.



- 761 Noji T.T., Rey F., Miller L.A., Borsheim K. Y., Urban-Rich J.: Fate of biogenic carbon in the upper
762 200 m of the central Greenland Sea. *Deep-Sea Res. II* 46, 1497-1509,
763 [https://doi.org/10.1016/S0967-0645\(99\)00032-6](https://doi.org/10.1016/S0967-0645(99)00032-6), 1999.
- 764 Norwegian Polar Institute: Sea ice extent in the Fram Strait in September. Environmental monitoring
765 of Svalbard and Jan Mayen (MOSJ). URL: [http://mosj.no/en/climate/ocean/sea-ice-extent-](http://mosj.no/en/climate/ocean/sea-ice-extent-barents-sea-fram-strait.html)
766 [barents-sea-fram-strait.html](http://mosj.no/en/climate/ocean/sea-ice-extent-barents-sea-fram-strait.html) (<https://mosj.no>), 2022.
- 767 Onarheim, I. H., Årthun, M., Teigen, S. H., Eik, K. J., & Steele, M.: Recent Thickening of the
768 Barents Sea ice cover. *GRL*, 51, e2024GL108225. <https://doi.org/10.1029/2024GL108225>,
769 2024.
- 770 Oudot, C., Gerard, R., Morin, P., Gningue, I.: Precise shipboard determination of dissolved oxygen
771 (Winkler procedure) for productivity studies with commercial system. *Limnol. Oceanogr.* 33,
772 146–150, <https://doi.org/10.4319/lo.1988.33.6part2.1646>, 1998.
- 773 Pettine, M., Capri, S., Manganelli, M., Patrolecco, L., Puddu, A., and Zoppini, A.: The Dynamics of
774 DOM in the Northern Adriatic Sea. *Estuarine, Coastal and Shelf Science*, 52, 471–489,
775 <https://doi.org/10.1006/ecss.2000.0752>, 2001.
- 776 Polyakov, I. V., Ingvaldsen, R. B., Pnyushkov, A. V., Bhatt, U. S., Francis, J. A., and Janout, M., et
777 al.: Fluctuating Atlantic inflows modulate Arctic Atlantification, *Science*, 381, 972-979,
778 <https://doi.org/10.1126/science.adh5158>, 2023.
- 779 Polyakov, I. V., et al.: Greater role for Atlantic inflows on sea-ice loss in the Eurasian Basin of the
780 Arctic Ocean. *Science* 356, 285-291. DOI:10.1126/science.aai8204, 2017.
- 781 Postel, L., Fock, H., and Hagen, W.: Biomass and abundance, *ICES Zooplankton Meth. Manual*,
782 83–192, <https://doi.org/10.1016/B978-012327645-2/50005-0>, 2000.
- 783 Priest, T., von Appen, W.J., Oldenburg, E., Popa, O., Torre-Valdés, S., Bienhold, C., et al.: Atlantic
784 water influx and sea-ice cover drive taxonomic and functional shifts in Arctic marine bacterial
785 communities. *ISME J.*, 17, 1612–1625, <https://doi.org/10.1038/s41396-023-01461-6>, 2023.
- 786 Putt, M., and Stoecker, D. K.: An experimentally determined carbon: volume ratio for marine
787 “oligotrichous” ciliates from estuarine and coastal waters, *Limnol. Oceanogr.*, 34, 1097-1107,
788 <https://doi.org/10.4319/lo.1989.34.6.1097>, 1989.
- 789 Rantanen, M., Karpechko, A.Y., Lipponen, A. et al.: The Arctic has warmed nearly four times faster
790 than the globe since 1979. *Commun Earth Environ* 3, 168. [https://doi.org/10.1038/s43247-022-](https://doi.org/10.1038/s43247-022-00498-3)
791 [00498-3](https://doi.org/10.1038/s43247-022-00498-3), 2022.
- 792 Relitti, F., Ogrinc, N., Giani, M., Cerino, F., Smodlaka Tankovic, M., Baricevic, A., Urbini, L.,
793 Krajnc B., Del Negro, P., De Vittor, C.: Stable carbon isotopes of phytoplankton as a tool to
794 monitor anthropogenic CO₂ submarine leakages. *Water*, 12, 3573.
795 <https://doi.org/10.3390/w12123573>, 2020.



- 796 Rudels, B., Friedrich, H. J., Quadfasel, D.: The Arctic Circumpolar Boundary Current, Deep-Sea
797 Res. Part II, 46, 1023-1062, [https://doi.org/10.1016/S0967-0645\(99\)00015-6](https://doi.org/10.1016/S0967-0645(99)00015-6), 1999.
- 798 Schlitzer, R.: Ocean Data View, <https://odv.awi.de>, 2024.
- 799 Simpkins, G.: Greenland Sea convection. *Nature Clim Change* 9, 7. [https://doi.org/10.1038/s41558-](https://doi.org/10.1038/s41558-018-0384-6)
800 [018-0384-6](https://doi.org/10.1038/s41558-018-0384-6), 2019.
- 801 Skjelvan, I., Olsen, A., Anderson, L. G., Bellerby, R. G. J., Falck, E., Kasajima, Y., Kivimäe, C.,
802 Abdirahman, O., Rey, F., Olsson, K. A., Johannessen, T., Heinze, C. A review of the inorganic
803 carbon cycle of the Nordic Seas and Barents Sea. In: Drange H. et al. (Eds.) *The Nordic Seas:*
804 *An Integrated Perspective Oceanography, Climatology, Biogeochemistry, and Modeling.*,
805 *Geophys. Monogr. Ser.*, vol. 158, pp. 157-175, AGU, Washington, D. C. 2005.
- 806 Smedsrud, L. H., Muilwijk, M., Brakstad, A., Madonna, E., Lauvset, S. K., Spensberger, C., et al.:
807 Nordic Seas Heat Loss, Atlantic Inflow, and Arctic Sea Ice Cover Over the Last Century, *Rev.*
808 *Geophys.*, 60, <https://doi.org/10.1029/2020RG000725>, 2022.
- 809 Throndsen, J.: Preservation and Storage, in: *Phytoplankton Manual*, edited by: Sournia, A., Unesco
810 Publishing, Paris, France, 69–74, 1978.
- 811 Urbini, L., Ingrosso, G., Djakovac, T., Piacentino, S., Giani, M.: Temporal and Spatial Variability
812 of the CO₂ System in a Riverine Influenced Area of the Mediterranean Sea, the Northern
813 Adriatic. *Front. Mar. Sci.*, 679, <https://doi.org/10.3389/fmars.2020.00679>, 2020.
- 814 Utermöhl, H.: Zur Vervollkommung der quantitativen Phytoplankton-Methodik. *Mitt Int Ver Theor*
815 *Angew Limn*, 9, 1-38, 1958.
- 816 van Guelpen, L., Markle, D. F., and Duggan, D. J.: An evaluation of accuracy, precision, and speed
817 of several zooplankton subsampling techniques, *ICES J. Mar. Sci.*, 40, 226–236,
818 <https://doi.org/10.1093/icesjms/40.3.226>, 1982.
- 819 Verity, P. G., Lagdon, C.: Relationship between lorica volume, carbon, nitrogen, and ATP content
820 of tintinnids in Narragansett Bay, *J. Plankton Res.*, 6, 859-868,
821 <https://doi.org/10.1093/plankt/6.5.859>, 1984.
- 822 von Bodungen, B., Antia, A., Bauerfeind, E. et al.: Pelagic processes and vertical flux of particles:
823 an overview of a long-term comparative study in the Norwegian Sea and Greenland Sea. *Geol.*
824 *Rundsch.* 84, 11–27, <https://doi.org/10.1007/BF00192239>, 1995.
- 825 Wang, X., Zhao, J., Hattermann, T., Lin, L., & Chen, P.: Transports and accumulations of Greenland
826 Sea intermediate waters in the Norwegian Sea. *Journal of Geophysical Research: Oceans*, 126,
827 e2020JC016582. <https://doi.org/10.1029/2020JC016582>, 2021.
- 828 Whitt, D. B.: Global Warming Increases Interannual and Multidecadal Variability of Subarctic
829 Atlantic Nutrients and Biological Production in the CESM1-LE, *Geophys. Res. Lett.*, 50,
830 <https://doi.org/10.1029/2023GL104272>, 2023.



- 831 Yergeau, E., Michel, C., Tremblay, J., Niemi, A., King, T. L., Wyglinski, J., et al.: Metagenomic
832 survey of the taxonomic and functional microbial communities of seawater and sea ice from the
833 Canadian Arctic, 10.1038/srep42242, *Sci. Rep.*, 7, 42242, 2017.
- 834 Zingone., A., Totti, C., Sarno, D., Cabrini, M., Caroppo, C., Giacobbe, M. G., Lugliè, A., Nuccio,
835 C., and Socal, G. Fitoplancton: metodiche di analisi quali-quantitativa, in: *Metodologie di studio*
836 *del plancton marino*, edited by: Socal, G., Buttino, I., Cabrini, M., Mangoni, O., Penna, A., and
837 Totti, C., *Manuali e Linee Guida ISPRA SIBM*, Rome, Italy, 213–237, 2010.